Thermal non-equilibrium transport in colloids

Alois Würger

Thermal non-equilibrium transport in colloids

Alois Würger
Laboratoire Ondes et Matière d'Aquitaine, Université Bordeaux 1 & CNRS,
351 cours de la Libération, 33405 Talence, France

A temperature gradient acts like an external field on colloidal suspensions and drives the solute particles to the cold or to the warm, depending on interfacial and solvent properties. We discuss different transport mechanisms for charged colloids, and how a thermal gradient gives rise to companion fields. Particular emphasis is put on the thermal response of the electrolyte solution: Positive and negative ions diffuse along the temperature gradient and thus induce a thermoelectric field which in turn acts on the colloidal charges. Regarding polymers in organic solvents, the physical mechanism changes with decreasing molecular weight: High polymers are described in the framework of macroscopic hydrodynamics, for short chains and molecular mixtures of similar size, the Brownian motion of solute and solvent becomes important.

PACS numbers:

Contents

I. INTRODUCTION

When applying a temperature gradient to a complex fluid, one observes relative motion of its components and relaxation towards a steady state with non-uniform concentrations [1]. The thermal gradient acts as a generalized force on suspended particles, molecules, droplets, or micelles, and drives them to the cold or to the warm; the drift velocity

$$\mathbf{u} = -D_T \boldsymbol{\nabla} T \tag{1}$$

depends on the surface properties of the solute and its interactions with the solvent [2, 3]. In the framework of non-equilibrium thermodynamics, the mobility D_T corresponds to an Onsager cross coefficient that describes the coupling between heat and particle flows.

In the last decade, a host of experimental studies on thermophoresis in macromolecular solutions and colloidal suspensions have revealed a rich behavior and often surprising dependencies on salinity and solute concentration [4–6], surface coating [7], and molecular weight [8–10]. Since in many cases the thermophoretic mobility D_T results from the competition of opposite mechanisms, neither its magnitude nor its sign can be predicted from simple rules; a minor change of one of the above parameters may reverse the transport velocity. Modern experimental techniques rely on single-particle tracking, Soret cells and thermogravitational columns, all-optical methods, and thermal field-flow fractionation; recent reviews are given by Wiegand [11] and Piazza & Parola [12].

Thermophoresis has been shown to provide an efficient separation technique for macromolecules in organic solvents [13], and has been used as a molecular trap for

DNA in a microchannel with ambient flow [14]. Microfluidic applications include colloidal accumulation [15] and confinement in thin films [16, 17]. Thermally driven crowding of nucleotides has been discussed as a possible mechanism in the molecular evolution of life [18, 19]. On an almost macroscopic scale, thermal forces may reshape 100-micron bicontinuous lyotropic crystals [20], and thermocapillary forces can be used for manipulating droplets and bubbles in microchannels [21–23].

A. To the cold or to the warm?

The thermophoretic mobility in (1) is defined such that positive values $D_T > 0$ occur for "thermophobic" solutes that move to the cold, whereas $D_T < 0$ corresponds to "thermophilic" behavior. As a most striking feature, various liquid suspensions show a change of sign as a function of an external control parameter. Studies on alkali halide solutions confirm Ludwig's and Soret's early measurements ($D_T > 0$) at room temperature [24, 25], yet find a negative salt mobility at lower T [26–31]; NaCl and KCl show a sharp drop from positive to negative values as the salinity approaches 100 mMol/l [30].

For charged latex beads in aqueous solution, Putnam and Cahill observed a change from thermophilic to thermophobic behavior as a function of the electrolyte composition; the particles move to the warm at high pH value but change direction when salt is added [5]. Low temperatures favor a negative mobility, as reported by Piazza and co-workers for polypeptides, SDS micelles, and DNA [32, 33]; a variety of colloidal suspensions show a universal temperature dependence. When adding polyethylene glycol to a suspension of polystyrene beads, Sano and collaborators observed a sign inversion and a strong enhancement of the Soret effect [15].

The thermophoretic mobility D_T of high polymers is independent of the molecular weight [3, 34–37], contrary to the Einstein coefficient which decreases with the inverse gyration radius. Recent studies show, however, that for chains of less than 100 repeat units, D_T varies with the length and may even become negative for very short molecules [8–10]. Stadelmaier and Köhler found moreover that specific solvent effects become important for short chains [10]. Rather generally, binary mixtures of small molecules show subtle dependencies on the molar mass and volume dependencies. For example, the mobilities of protonated and deuterated benzene in cyclohexane show a significant isotope effect and even take opposite signs at a given concentration [38].

B. Physical mechanisms - an overview

Colloidal particles in liquid suspension interact with the solvent mainly through electric double-layer and dispersion forces; the presence of an additional molecular solute, such as in colloid-polymer mixtures, may give rise to depletion forces. In a temperature gradient these interactions induce thermoosmotic flows [39, 40], similar to electrokinetic phenomena that occur in an applied electric field. Here we give an overview of the physical mechanisms.

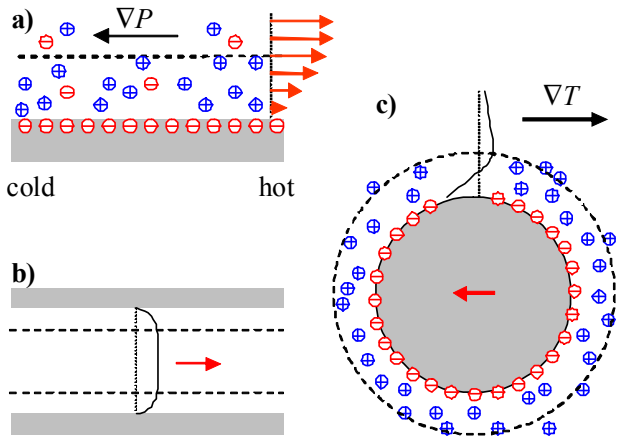

FIG. 1: (a) Thermoosmotic flow in the electric double layer close to a negatively charged surface. The pressure in the boundary layer is slightly higher at the cold side and drives the charged liquid to the warm; the resulting velocity profile reaches its maximum value beyond the screening length, which is indicated by the dashed line. (b) Thermoosmosis along the charged walls drives the fluid to the hot end of the microchannel; the solid line indicates the velocity profile. (c) A charged bead with its diffuse layer in a temperature gradient. The solid line indicates the fluid velocity profile in the laboratory frame. The particle moves to the left, the flow changes sign within the boundary layer and reaches its maximum velocity beyond the screening length, before slowly decaying at larger distance.

Thermoosmosis in the electric double layer. Since most solute and solvent properties depend on temperature, a thermal gradient modifies the electric double layer in many ways. The dominant effect arises from the excess hydrostatic pressure within the diffuse layer. Fig. 1a illustrates how a temperature gradient affects the electric double layer close to a flat surface. The number densities of positive and negative ions differ from their bulk value by $n_\pm$; these excess ions result in an additional pressure $P = (n_+ + n_-)k_BT$ that vanishes well beyond the Debye length. The total change $n_+ + n_-$ is positive, and so is the excess pressure. At each spot of the charged surface the ion densities are in local equilibrium according to the Poisson-Boltzmann expression $n_\pm = n_0(e^{\mp e\psi/k_BT} - 1)$ with the electrostatic potential ψ. Yet in a non-uniform temperature, P slowly varies along the boundary; because of the exponential factors, the pressure is slightly higher at the cold side, and its gradient is opposite to $\boldsymbol{\nabla} T$. As a consequence there is a flow of charged liquid along the surface towards higher temperature; the velocity profile is maximum at a distance beyond one Debye length. This stationary flow arises from the balance of

osmotic pressure and viscous forces; it doesn't reach an equilibrium state as long as the external field $\boldsymbol{\nabla} T$ is kept at a finite value.

Fig. 1b shows how, in an open microchannel between two reservoirs at different T, the thermoosmotic flow drives the fluid to the hot end of the tube [39, 40]; note the flat velocity profile in the core. A schematic view of the screening layer of a negatively charged bead is given in Fig. 1c. The boundary velocity beyond the Debye length has to be matched to the far field; one finds that the fluid beyond the boundary layer and the particle move in opposite directions. The rather intricate velocity profile with respect to the laboratory frame is indicated by the solid line in the upper part. The particle moves to lower temperatures with

$$\mathbf{u} = -\frac{\varepsilon \zeta^2}{3\eta} \frac{\boldsymbol{\nabla} T}{T}, \tag{2}$$

where ε and η are the solvent permittivity and viscosity [41, 42]. The variation with the square of the surface potential ζ was first derived by Ruckenstein [2], by exploiting analogies with colloidal electrophoresis and the Marangoni effect. A refined analysis reveals the existence of additional terms arising from the temperature dependence of solvent parameters such as permittivity and salinity [41–43]. Eq. (2) describes the case of large ζ-potential; an additional factor $\frac{1}{4}$ occurs in the opposite limit. Typical velocities in a thin film or microchannel attain values of several μm/s.

Thermoelectric effect. From Ruckenstein's result one would expect all colloidal solutes to move to the cold, whereas the above mentioned experiments indicate that there is no such general rule. This contradiction is resolved when accounting for the thermoelectric response of the electrolyte solution [5]: The thermal gradient drives positive and negative salt ions at different strength or even in opposite directions, depending on their size and solvation energy [44]. In the steady state of a closed system, where the ion currents vanish, an electrostatic thermopotential $(\Delta T/T)\psi_0$ develops between the hot and cold boundaries of the vessel due to their temperature difference ΔT. The corresponding bulk electric field $-(\psi_0/T)\boldsymbol{\nabla} T$ acts on the suspended particles; with the Helmholtz-Smoluchowski electrophoretic mobility $\varepsilon\zeta/\eta$ one obtains the velocity

$$\mathbf{u} = -\frac{\varepsilon \zeta \psi_0}{\eta} \frac{\boldsymbol{\nabla} T}{T}. \tag{3}$$

Its sign depends on the surface and thermoelectric potentials [5, 42]. Most colloids are negatively charged, with numerical values for ζ ranging from -10 to -100 mV. The thermopotential parameter of common electrolytes is of the same order of magnitude but may take both signs, e.g. $\psi_0 = -15$ mV for NaCl and $+70$ mV for NaOH at room temperature. Thus the thermoelectric velocity (3) may overtake the Ruckenstein term (2) and drive the particle to the hot side.

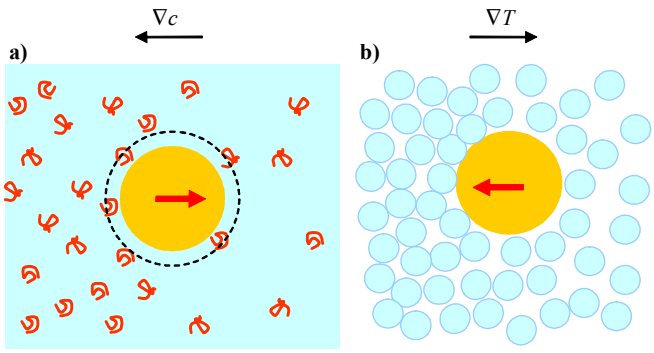

FIG. 2: a) Depletion forces in a colloid-polymer mixture. The gyration radius of a polymer results in an excluded volume around a spherical bead, as indicated by the dashed line. This entropic repulsion pushes the particle to lower polymer concentration, opposite to ∇c. b) Particle suspended in a molecular liquid with non-uniform number density $\nabla n = -n\beta\nabla T$. The dispersion forces attract the particle in regions of higher density, that is, to the cold side of the sample.

Thermally driven depletion forces. Both static and transport properties of colloid-polymer mixtures are sensitive to depletion forces. As illustrated in Fig. 2a, in a polymer solution of non-uniform concentration c, the particles migrate towards regions of low dilution [45]. Because of the excluded volume of a polymer coil of gyration radius R, the overall configurational entropy increases as the particle diffuses to lower c, resulting in a mean velocity opposite to $\boldsymbol{\nabla} c$ [46],

$$\mathbf{u} = -\frac{k_B T R^2}{3\eta} \boldsymbol{\nabla} c. \tag{4}$$

A similar effect occurs when applying a temperature gradient to a colloid-polymer mixture: The Soret motion of the polymer imposes a non-uniform concentration $\boldsymbol{\nabla} \ln c = -\alpha \boldsymbol{\nabla} \ln T$ [35]. Most polymers accumulate in regions of lower temperature ($\alpha > 0$) and thus drive the particles towards the warm; the resulting velocity may exceed the above mechanisms (2) and (3) by two orders of magnitude [15].

Dispersion forces. The van der Waals interaction dominates for particles suspended in simple liquids. Since molecular dispersion forces depend little on temperature, the thermoosmotic flow along a solid-liquid interface is mainly due to the solvent density gradient. Except for water below 5° C, simple liquids expand upon heating. Because of the higher density, a given volume element at the cold side is more strongly attracted by the particle than at the hot side, resulting in a solvent flow along the surface towards higher T. This leads to an opposite motion of suspended particles or macromolecules. As shown in Fig. 2b, the solute is dragged in regions of higher density, that is, towards the cold; its velocity

$$\mathbf{u} = -\frac{2\beta H}{9\pi\eta d_0} \boldsymbol{\nabla} T \tag{5}$$

depends on the solvent thermal expansivity β, the Hamaker constant H of the solute-solvent interaction, and a molecular length scale d_0. This velocity is independent of the particle size or, in the case of high polymers, of the molecular weight [3, 35]. With typical parameters and a gradient of one Kelvin per micron one finds velocities of several μm/s.

Thermal diffusion. So far we have treated the particle as a macroscopic body and the surrounding liquid as a continuous medium. The above expressions (2-5) arise from balancing the particle-solvent forces with the viscous stress in the boundary layer. As pointed out by Brenner [47] and Astumian [48], this macroscopic hydrodynamics approach neglects both Brownian motion of the solute and the molecular structure of the solvent.

We address one aspect that is particularly important for small solutes and that arises from the very non-equilibrium nature of thermophoresis. In addition to the solute-solvent interactions that are treated in (2)–(5), Onsager's generalized forces comprise terms that derive from the solvent-solvent forces, and that become relevant for small solutes. In a binary mixture of molecular beads of radius a, mobility $1/6\pi\eta a$, and molecular enthalpies $h_i < 0$, the velocity of species 1 takes the form

$$\mathbf{u}_1 = \frac{h_1 - h_2}{6\pi\eta a}\frac{\boldsymbol{\nabla} T}{T}. \tag{6}$$

The two terms in the numerator have a simple physical meaning in terms of the flow of enthalpy along a temperature gradient [1]. Because of its negative sign, h_1 drives the solute bead "1" to lower T. Yet this implies the opposite motion of a solvent molecule, which itself would rather diffuse to the cold with strength h_2. Thus the enthalpy difference accounts for the competition of the molecular components that are both attracted by lower temperatures. Discarding h_2, noting $h_1 \sim -H$ for dispersion forces, and replacing a with d_0, one readily recovers the expression (5) for a large solute. Experiments suggest that the "enthalpies of transfer" depend in a subtle manner on molecular parameters such as weight, size, and polarity.

C. Thermally driven motion in gases

Though this article is concerned with thermophoresis in liquids, a brief reminder of what is known for gasses phases seems useful. Depending on the size of the solute, temperature-driven motion in gases is described by surface creep flow or thermal diffusion. Both mechanisms turn out to be relevant for liquids, albeit lead to a more complex behavior than in gases: Whereas the collisions of free molecules are well accounted for by kinetic theory, there is no such general description for the molecular forces in a liquid phase.

In 1870 Tyndall observed that dust particles suspended in air were repelled from a heated surface; the dust depleted zone appeared as dark space in a light scattering experiment [49]. A few years later, Crookes found a related effect in his radiometer experiment, where a vertically mounted lightmill starts rotating if its vanes are heated at one side [50]. The subsequent analysis by Reynolds and Maxwell in terms of kinetic gas theory pointed out the existence of a thermal creep flow along a solid surface with a non-uniform temperature [51, 52]. Regarding a microchannel between two reservoirs at equal pressure but different temperature, one observes a gas flow towards the hot end, or "thermal transpiration". Similarly, the gas at the surface of a suspended particle creeps to higher temperature, resulting in an opposite drift velocity of the particle,

$$u = -\frac{3\eta}{4\rho}\frac{\nabla T}{T}, \tag{7}$$

where η is the dynamic viscosity and ρ the mass density of the gas. As illustrated in Fig. 3a, thermal creep is confined to a layer of about one mean free path $\ell_m = 2\eta/\rho c$ that depends on the kinematic viscosity η/ρ and the molecular velocity c; for common gases it is of the order of 70 nm.

Maxwell's expression (7) neglects heat transport through the particle. By matching the temperature field and the heat flux at the surface, Epstein found that the drift velocity depends on the ratio of particle and gas thermal conductivities κ_P and κ_G according to $u/(1 + \kappa_P/2\kappa_G)$ [53]. Eq. (7) has been derived for large Knudsen number, that is, for a particle radius much bigger than the mean free path, $a \gg \ell_m$. It turns out that, up to numerical prefactors, this result remains valid in the opposite limit [54]. Minor corrections occur for non-spherical particles and non-specular reflection at the surface [55]. In any case the suspended particle migrates to the cold.

A different situation is encountered in binary molecular mixtures. From the kinetic theory developed by Enskog and Chapman [56–58], a particularly simple result arises for hard spheres of equal radius but unlike masses: To linear order in the mass difference, the velocity of species 1 reads as [59]

$$u_1 = -D\frac{105}{118}\frac{m_1 - m_2}{m_1 + m_2}\frac{\nabla T}{T}. \tag{8}$$

This means that, of two otherwise identical molecules, the heavier one moves to the cold and the lighter one to the warm. When noting the relation $D = \frac{6}{5}\eta/\rho$ between the diffusion coefficient and the kinematic viscosity of ideal gases, one finds that, for heavy solute molecules $m_1 \gg m_2$, Eq. (8) essentially reduces to Maxwell's expression. In the case of equal mass but different size, a similar relation is obtained in terms of the molecular radii, $u_1 \propto -(a_1 - a_2)$, such that the larger molecule moves to the cold side [59]. The mass effect can be used for isotope separation [60], as verified for ammonia $^{14}NH_3/^{15}NH_3$ [61]. Waldmann's thermal diffusion data on mixtures of dimer molecules such as H_2, D_2, N_2, O_2 compare favorably with the theoretical values [62].

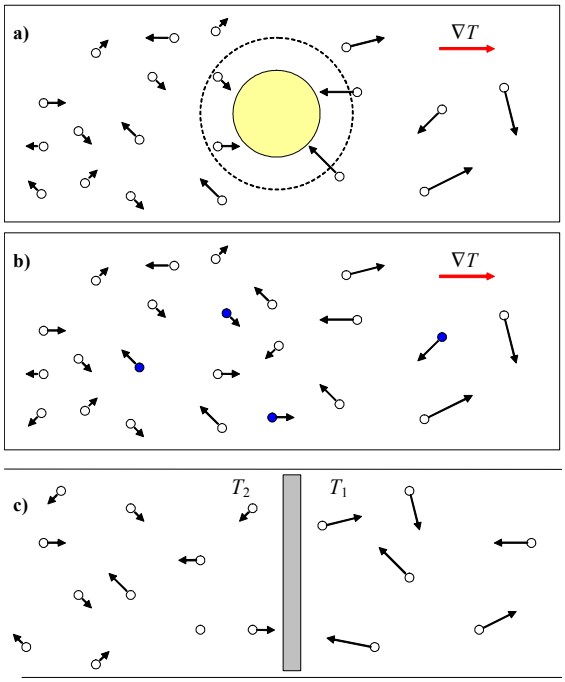

FIG. 3: a) Particle suspended in a gas with a temperature gradient ∇T. The dashed circle indicates the distance corresponding to the molecular mean free path ℓ_m. Within this layer there is a creep flow to higher temperature; accordingly the particle moves to the left towards lower T. b) Binary molecular mixture; according to (8) the smaller and lighter species migrates towards higher temperatures. c) Rayleigh piston separating two gases at equal pressure but different temperatures $T_2 < T_1$. The piston of mass M moves freely in horizontal direction and shows Brownian motion due to the molecular collisions. The temperature asymmetry rectifies the random motion of the piston which, as a consequence, moves to the right towards higher temperatures.

The sign of the drift velocity (8) is closely related to Brownian motion in a temperature gradient, or *thermal diffusion*. Indeed, the velocity fluctuations $\langle v^2 \rangle \sim k_B T/m$ vary with the inverse mass. Large and heavy particles may be treated as macroscopic objects, that are driven to the cold by thermal creep flow. On the other hand, small and light species are subject to large fluctuations and may diffuse to higher temperatures.

The role of solute Brownian motion is highlighted by a thought experiment discussed by Lieb [63]. Fig. 3c illustrates a modified version that was studied in Refs. [64, 65]: A structureless Rayleigh piston separates two ideal gases at the same pressure P but different temperatures $T_1 > T_2$. If the piston is much heavier than the gas molecules, it hardly shows velocity fluctuations. Then the momentum transfer from both sides cancels in the average; collisions with molecules coming from the left side transfer less momentum in the average, yet are more frequent because of the higher density $n_2 = n_1(T_1/T_2)$. As a consequence, there is no net force and the piston remains immobile. A more complex situation arises for a piston of finite mass M, not much larger than that of the gas molecules m; since the gas does not pass at the piston's edges, this corresponds to a suspended particle without thermal creep. The asymmetric temperature profile rectifies the velocity fluctuations $\langle \hat{u}^2 \rangle \sim k_B T/M$, resulting in a finite mean velocity $u = \langle \hat{u} \rangle$. Accounting for energy and momentum conservation, one finds to leading order in $\sqrt{m/M}$ [64, 65]

$$u = \sqrt{\frac{\pi}{8}\frac{m}{M}}\left(\sqrt{\frac{k_B T_1}{M}} - \sqrt{\frac{k_B T_2}{M}}\right). \tag{9}$$

Its Brownian motion drives the piston towards higher temperature, that is, to the right in Fig. 3c. The velocity u vanishes as the mass ratio m/M tends towards zero.

Eqs. (7)–(9) exemplify two basically different physical mechanisms. The first one corresponds to the usual definition of *thermophoresis*. It relies on a hydrodynamic treatment of thermal creep in the boundary layer and prevails for large particles, in close analogy to Eqs. (2)–(5) for liquid suspensions. The second mechanism arises from rectification of Brownian motion in a non-uniform temperature profile and leads to $u > 0$. In a gas mixture this *thermal diffusion* becomes relevant if the masses of solute and solvent molecules are not too different, as illustrated by (8).

D. Solute accumulation and confinement

Separating and mixing the components of a complex fluid are important issues in microfluidics. Electrophoresis and optical tweezer body forces [66] are common techniques for manipulating colloids. In recent years thermal gradients have been shown to provide an alternative; they have been used for creating both lateral and parallel force field in microchannels and in thin films. With typical temperature gradients of the order of K/μm, the transport velocity (1) takes values of several microns per second. Like electrophoresis, thermally driven motion of large solutes is independent of their size [67], whereas optical-tweezer forces vary with the particle volume.

The out-of-equlibrium solute current consists of the thermophoretic part and diffusion with the Einstein coefficient D [1],

$$\mathbf{J} = -nD_T \boldsymbol{\nabla} T - D\boldsymbol{\nabla} n, \tag{10}$$

where n is the number of particles per unit volume. The steady state is characterized by $\mathbf{J} = 0$. When taking the coefficients D_T and D as constants, the non-uniform stationary density is readily integrated,

$$n(\mathbf{r}) = n_0 e^{-S_T \Delta T(\mathbf{r})}, \tag{11}$$

where ΔT is the spatial temperature modulation; the Soret coefficient

$$S_T = D_T/D \tag{12}$$

is defined as the ratio of thermophoretic and Einstein coefficients. For micron-sized colloidal particles or polymers of molecular weight $M_w = 10^5$, typical values of S_T range from 0.03 K^{-1} to 0.2 K^{-1}. Thus a temperature difference of $\Delta T = 25$ K results in a concentration ratio in cold and hot spots by two orders of magnitude. This accumulation factor can still be enhanced, e.g., by coupling to a convective flow [68, 69], or by depletion forces due to an additional molecular solute [15]. The mobility D_T is independent of the solute size, whereas the diffusion coefficient is proportional to the inverse particle radius, or gyration radius in the case of polymer. Thus solutes of different size but identical surface properties, have the same transport velocity but differ in their stationary state.

In analogy to the sedimentation length $\ell = k_B T/mg$ of suspended particles with excess mass m, the steady state in a constant temperature gradient is described by a characteristic length

$$\ell = D/u. \tag{13}$$

A thermal gradient perpendicular to a confining wall results in a stationary density $n \propto e^{-z/\ell}$, where z is the distance from the solid boundary. With typical parameters for micron-sized particles, $D \sim \mu m^2/s$ and $u \sim \mu m/s$, one finds that the length ℓ is comparable to the particle size; thus the non-uniform temperature provides an efficient means of confinement. Contrary to gravity that requires a sufficiently large buoyancy force, thermally driven confinement is independent of the mass and works equally well for particles and polymers.

II. CHARGED COLLOIDS

A. Boundary layer approximation

Motion on micron or nanometer scales in a liquid is governed by low-Reynolds number hydrodynamics. The velocity field $\mathbf{v}$ of an incompressible fluid ($\boldsymbol{\nabla} \cdot \mathbf{v} = 0$) is solution of the stationary Stokes equation,

$$\eta \boldsymbol{\nabla}^2 \mathbf{v} = \boldsymbol{\nabla} P - \mathbf{f}, \tag{14a}$$

where η is the viscosity, P the hydrostatic pressure, and $\mathbf{f}$ the force density exerted by a suspended particle on the surrounding fluid.

Depending on the ratio of the particle radius a and the range B of the force field, there are two schemes for an approximate solution of Stokes' equation. If $a \gg B$, the particle surface may be considered as flat in the range where the force $\mathbf{f}$ is significant; the boundary-layer approximation takes advantage of this separation of length scales [70]. If on the contrary, the particle-solvent interactions are of long range ($B \gg a$), an appropriate starting point is provided by the counterforce acting on the particle, that is the volume integral of $-\mathbf{f}$ [71]; this Hückel limit is discussed in Sect. III below.

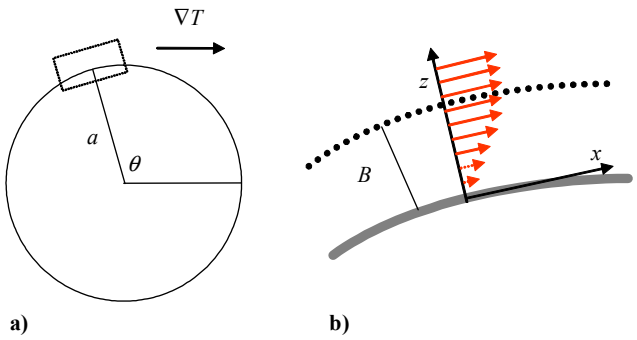

FIG. 4: Schematic view of a spherical particle in a thermal gradient (a) and of the boundary layer approximation (b). Due to the solute-solvent interactions, the fluid velocity relative to the particle surface increases and attains the value v_B at distances beyond the interaction range B.

Here we consider the case where the particle radius is much larger than the interaction range B, closely following Anderson [70]. In this case hydrodynamic quantities vary slowly along the particle, and much more rapidly in vertical direction. It turns out convenient to adopt local coordinates x and z attached to the surface, as shown in Fig. 4. Close to the particle, the perpendicular velocity component vanishes, $v_z = 0$, whereas the parallel velocity hardly depends on the coordinate x, that is, in leading order one has $v_x = v_x(z)$. As a consequence, the normal component of Stokes' equation reads

$$0 = \frac{dP}{dz} - f_z. \tag{14b}$$

Its integral gives the excess hydrostatic pressure P, which is defined such that it vanishes far from the particle. The parallel component simplifies to

$$\eta \frac{d^2 v_x}{dz^2} = \frac{dP}{dx} - f_x. \tag{14c}$$

This relation is integrated with Stokes boundary conditions. The velocity is zero at the solid surface, $v_x|_{z=0}$, and takes a constant value at B. Thus the first integral of this differential equation disappears at the upper bound, $dv_x/dz|_{z=B} = 0$, and the second integral results in [70]

$$v_B = \frac{1}{\eta} \int_0^B dz z \left(f_x - \frac{dP}{dx} \right). \tag{15}$$

In this article we discuss several examples where the force f_x or the local pressure gradient $\partial_x P$, or both are finite.

In general the perpendicular components f_z and $\partial_z P$ are much larger than the parallel ones. For a homogeneous surface both the force density f_x and the pressure derivative $\partial_x P$ vary with the sine of the polar angle, and so does the boundary velocity (15),

$$v_B = \bar{v}_B \sin\theta,$$

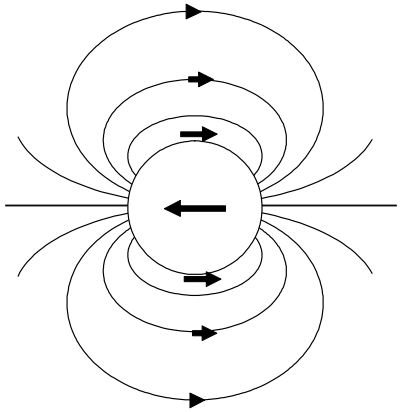

FIG. 5: Fluid velocity field $\mathbf{v}(\mathbf{r})$ with respect to the laboratory frame, in the vicinity of a particle with quasislip velocity $v_B = -\frac{3}{2}u\sin\theta$. The detail of the boundary layer of Fig. 4b is not visible on this scale.

with the maximum value $\bar{v}_B$ occurring at the midplane $\theta = \frac{\pi}{2}$. The resulting particle velocity u is opposite to the osmotic flow in the boundary layer; performing the orientational average over the surface $\mathbf{u} = -\langle v_B \mathbf{e}_x \rangle$ one finds [70]

$$u = -\frac{2}{3}\bar{v}_B. \tag{16}$$

As illustrated in Fig. 4b, the boundary velocity v_B gives the relative speed of the particle and the fluid beyond the interaction length. This implies that in the laboratory frame, the fluid at the midplane moves in the opposite direction with velocity $\frac{1}{3}\bar{v}_B$.

The velocity field at large distances is obtained by matching the general solution of the force-free Stokes' equation with the boundary value $v_B = -\frac{3}{2}u\sin\theta$,

$$\mathbf{v}(\mathbf{r}) = u\frac{a^3}{r^3}\left(\frac{1}{2}\sin\theta\mathbf{t} + \cos\theta\mathbf{n}\right). \tag{17}$$

The normal and tangential unit vectors are those derived from polar coordinates with the origin at the center of the particle; thus $\mathbf{n}$ and $\mathbf{t}$ are directed along the positive z-axis and the negative x-axis, respectively. The vector field $\mathbf{v}(\mathbf{r})$ is shown in Fig. 5 for $u < 0$, that is, for the particle migrating to the left. As its most remarkable properties, the orientational average over a sphere of given radius r vanishes, $\langle \mathbf{v}(\mathbf{r}) \rangle = 0$, and there is no "backflow": Integrating (17) over the plane $\theta = \frac{\pi}{2}$, one obtains the fluid current $-\pi a^2 u$, which exactly cancels that of the particle [72].

B. Double-layer forces

Formally the transport velocity of a suspended particle is given by Eqs. (15) and (16) in terms of the solute-solvent force field. Here we discuss in detail the physical origin of thermoosmotic flow in a charged double-layer and calculate the resulting particle velocity. Consider a spherical particle of radius a and surface charge density $e\sigma$. The electrostatic potential ψ and the corresponding electric field $\mathbf{E} = -\boldsymbol{\nabla}\psi$ are screened through the accumulation of mobile counterions in the electrolyte. In Poisson-Boltzmann mean-field approximation, the excess densities of (monovalent) positive and negative ions are given by

$$n_\pm = n_0(e^{\mp e\psi/k_BT} - 1),$$

where n_0 is the bulk salinity. Due to the accumulation of counterions and the depletion of co-ions, the fluid in the boundary layer carries a charge density ρ and an excess density n of mobile ions,

$$\rho = e(n_+ - n_-), \quad n = n_+ + n_-. \tag{18}$$

These quantities are finite within the charged double layer only. At larger distances they decay exponentially, on a scale given by the Debye length

$$\lambda = (8\pi n_0 \ell_B)^{-\frac{1}{2}} \tag{19}$$

where $\ell_B = e^2/4\pi\varepsilon k_B T$ is the Bjerrum length and ε the solvent permittivity.

In an isotropic system, the properties of the electric double layer depend only on the distance from the particle. An applied electric field, or a chemical or thermal gradient, breaks the spherical symmetry, induces lateral forces on the ions in the electric double layer, and thus moves the fluid with respect to the particle surface. Throughout this article we consider weak perturbations; that is, we use linear response theory and evaluate the driving force $\mathbf{f}$ and the hydrostatic pressure gradient $\boldsymbol{\nabla}P$ to first order in the external fields. This scheme is valid as long as the parameters vary little over the size a of the suspended particle.

We briefly address the *non-equilibrium* character of thermoosmosis. Like previous studies on electrophoresis and diffusiophoresis [70], we assume that local equilibrium is established in the double layer of thickness $\lambda \ll a$. More precisely, this means that the above expressions for the ion densities $n_\pm$ are valid at any spot of the charged surface as a function of the vertical coordinate z in Fig. 4b. Parallel to the surface along the x-axis, however, the system is out of equilibrium. The gradients of slowly varying parameters such as T and n_0, provide the thermodynamic forces acting on the electric double layer; the system does not reach equilibrium as long as the experimental setup keeps these gradients constant.

Now we derive the force density and the pressure gradient appearing in Stokes' equation (14a). The force $\mathbf{f}(\mathbf{r})dV$ exerted on a volume element dV of the fluid in the double layer contains two terms,

$$\mathbf{f} = \rho\bar{\mathbf{E}}_0 + \boldsymbol{\nabla}\cdot\mathcal{T}, \tag{20}$$

where the first one accounts for the coupling of the charge density to the external electric field $\mathbf{E}_0$; the bar indicates the deformation due to the permittivity jump

at the particle-fluid interface as discussed below. The second term is the divergence of the Maxwell tensor $\mathcal{T}_{ij} = \varepsilon E_i E_j (1 - \frac{1}{2}\delta_{ij})$, which arises from the electric field $\mathbf{E} = -\boldsymbol{\nabla}\psi$ of the charged particle. Using the relation between the displacement vector and the charge density, $\rho = \boldsymbol{\nabla} \cdot \varepsilon \mathbf{E}$, and noting that the curl of $\mathbf{E}$ vanishes, one obtains [73, 74]

$$\boldsymbol{\nabla} \cdot \mathcal{T} = -\rho \boldsymbol{\nabla}\psi - \frac{1}{2} E^2 \boldsymbol{\nabla}\varepsilon. \tag{21}$$

Thus $\boldsymbol{\nabla} \cdot \mathcal{T}$ comprises the electric force exerted by the particle on the mobile ions and an electrostrictive term proportional to the permittivity gradient.

The excess ion density in the double layer increases the hydrostatic pressure by $P = nk_BT$. This excess pressure varies rapidly in normal direction, because of the screened electrostatic potential ψ, and slowly along the particle surface due to the non-uniform solvent parameters. When inserting the above expression for n and evaluating the gradients, we find

$$\boldsymbol{\nabla} P = -\rho \boldsymbol{\nabla}\psi + (\rho\psi + nk_BT) \frac{\boldsymbol{\nabla} T}{T} + nk_BT \frac{\boldsymbol{\nabla} n_0}{n_0}.$$

Gathering the inhomogeneous terms at the right-hand side of Stokes' equation we have [42],

$$\begin{aligned} \mathbf{f} - \boldsymbol{\nabla} P \;=\; & -(\rho\psi + nk_BT) \frac{\boldsymbol{\nabla} T}{T} \\ & - \frac{E^2}{2} \boldsymbol{\nabla}\varepsilon - nk_BT \frac{\boldsymbol{\nabla} n_0}{n_0} + \rho \bar{\mathbf{E}}_0. \end{aligned} \tag{22}$$

The rapidly varying terms $\rho\boldsymbol{\nabla}\psi$ have disappeared, and the total force acting on the electric double layer is given by the field $\bar{E}_0$ and the gradients of the slowly varying macroscopic solvent parameters T, ε, n_0. (The present notation slightly differs from that of Refs. [42, 75], where the gradient of the osmotic pressure is already included in the force density $\mathbf{f}$.) The total force field (22) satisfies the vertical component of Stokes' equation (14b) to leading order in the small parameter λ/a; in the following we integrate the parallel component (14c).

In this paper the electric field $\bar{E}_0$ is a companion field of $\boldsymbol{\nabla} T$, resulting from the electrolyte properties. For the thermoelectric effect to be discussed below, it is of the order of $k_B \nabla T/e$; typical experimental conditions give values ranging from 10^{-4} to 1 V/m. Thus $\bar{E}_0$ is much smaller than the field due to the charges at the particle surface, $E \sim 100$ V/m. All terms in (22) are of comparable size, and therefore by several orders of magnitudes smaller than E. As a result, Eq. (22) is much smaller than the intrinsic double layer forces; this justifies the use of linear-response approximation for the external perturbation.

In view of Eq. (15), only the force component parallel to the surface is relevant. Because of the different material properties of particle and fluid, the external fields are modified close to the interface. For example, electrostatic boundary conditions require that the parallel electric field and the normal component of the displacement vector be continuous at the interface; thus one finds the field along the particle surface

$$\bar{E}_{0x} = \frac{3\varepsilon_S}{2\varepsilon_S + \varepsilon_P} E_0 \sin\theta. \tag{23}$$

The permittivity of water being much larger then that of the particle, $\varepsilon_S \gg \varepsilon_P$, the field is parallel to the interface and its amplitude $\bar{E}_{0x} = \frac{3}{2} E_0 \sin\theta$ is enhanced by a factor $\frac{3}{2}$ with respect to the bulk value.

Similarly, the applied temperature gradient $\boldsymbol{\nabla} T$ is deformed if the heat conductivities κ_S and κ_P are different from each other [53]. Imposing continuity both on temperature and on the normal heat flux $\kappa \partial_z T$, results in the local parallel component

$$\frac{dT}{dx} = \frac{3\kappa_S}{2\kappa_S + \kappa_P} \nabla T \sin\theta. \tag{24}$$

Since most materials satisfy $\kappa_S \approx \kappa_P$, this effect is rather weak, and dT/dx is simply the projection of ∇T on the particle surface. Accordingly, the prefactor in (24) is put to unity throughout this article. (Metal particles constitute a noteworthy exception: Because of their high heat conductivity, they strongly reduce the local temperature gradient [76].) Finally, the projection of a constant bulk salinity gradient ∇n_0 on the particle surface reads as $dn_0/dx = \nabla n_0 \sin\theta$.

C. Transport velocity

The electric force $\mathbf{f}$ and the pressure gradient ∇P shear the charged fluid in the boundary layer, and the resulting thermoosmotic flow along the solute surface gives rise to the flow pattern shown in Figs. 1, 4, and 5. Before evaluating the corresponding transport velocity, we have to specify the electrostatic potential of the charged particle. To leading order in the small parameter λ/a, it is determined by the one-dimensional Poisson-Boltzmann equation $\varepsilon \partial_z^2 \psi = -\rho$, with the charge density given in (18). Its solution is well-known [71], and can be written in terms of the inverse hyperbolic tangent function,

$$\psi(z) = \zeta \, \mathrm{artanh}(e^{-z/\lambda}),$$

where ζ is the surface potential and λ the Debye length.

The parallel component of Stokes' equation is solved by Eq. (15). Performing the integral with the force density $f_x - \partial_x P$ given in (22), one obtains the boundary velocity

$$\begin{aligned} v_B \;=\; & \frac{\varepsilon(\zeta^2 - 3\zeta_T^2)}{2\eta T} \frac{dT}{dx} \\ & - \frac{\varepsilon \zeta_T^2}{2\eta} \left(\frac{1}{\varepsilon} \frac{d\varepsilon}{dx} + \frac{1}{n_0} \frac{dn_0}{dx} \right) - \frac{\varepsilon\zeta}{\eta} \bar{E}_{0x}, \end{aligned} \tag{25}$$

with the shorthand notation

$$\zeta_T^2 = \left(\frac{2k_BT}{e} \right)^2 2 \ln\cosh \frac{e\zeta}{4k_BT}.$$

In the framework of Poisson-Boltzmann theory, the surface potential reads

$$\zeta = \frac{2k_BT}{e}\,\mathrm{arsinh}(2\pi\sigma\ell_B\lambda), \tag{26}$$

where σ is the number density of elementary charges and $\ell_B \approx 7$ Å the Bjerrum length. Since mean-field theory ceases to be valid close to the particle, the surface potential is often considered as an effective quantity to be inferred from experiment. Both static and kinetic properties of the double layer are affected by charge correlations, hydration, and specific ion effects, which may modify the value of ζ [71, 77]. For values of the order of unity, the arsinh function varies logarithmically with its argument; thus a rough estimate for many colloidal systems is provided by $\zeta \sim 2k_BT/e$, which takes a value of about 50 mV.

The boundary velocity v_B varies along the particle surface with the polar angle as $\sin\theta$. Simplifying the permittivity and thermal conductivity ratios in the local electric field and temperature gradient, $\varepsilon_P \ll \varepsilon_S$ and $\kappa_P \approx \kappa_S$, and inserting (16), one readily obtains the drift velocity,

$$\begin{aligned}\mathbf{u} \;=\; & -\frac{\varepsilon(\zeta^2-3\zeta_T^2)}{3\eta}\frac{\boldsymbol{\nabla}T}{T} \\ & +\frac{\varepsilon\zeta_T^2}{3\eta}\left(\frac{\boldsymbol{\nabla}\varepsilon}{\varepsilon}+\frac{\boldsymbol{\nabla}n_0}{n_0}\right)+\frac{\varepsilon\zeta}{\eta}\mathbf{E}_0.\end{aligned} \tag{27}$$

This is the general expression for a charged particle subject to gradients of the solvent parameters T, ε, n_0. The last term gives the velocity induced by an electric field $\mathbf{E}_0$, with the Helmholtz-Smoluchowski mobility $\varepsilon\zeta/\eta$.

We discuss the physical origin of the first term, proportional to $\boldsymbol{\nabla}T$. The lateral force along the particle surface arises since the electric double layer in a thermal gradient is not isotropic: The excess pressure and the electrostatic energy density vary along the particle surface, and result in thermoosmotic flow in the electric double layer towards higher temperature. As shown in Fig. 1b, in a microchannel this quasislip velocity gives rise to an overall flow to the hot side, whereas a mobile particle is dragged in the direction opposite to the thermal gradient.

Thermoosmosis along a charged surface has first been discussed by Derjaguin in terms of enthalpy flow [40]; this picture is supported by the fact that the expression $\rho\psi + nk_BT$ in (22) corresponds to the double-layer enthalpy density. A detailed comparison reveals that the velocity contributions proportional to ζ^2 and ζ_T^2 stem from $\rho\psi$ and nk_BT, respectively. As illustrated in Fig. 1c, the particle moves to the cold side, i.e., the resulting velocity component is always opposite to $\boldsymbol{\nabla}T$. Indeed, the definition of ζ_T implies the inequality

$$\zeta^2 - 3\zeta_T^2 > 0.$$

For highly charged particles one finds $\zeta_T \ll \zeta$, resulting in the expression (2) given in the introduction. On the other hand, from the Debye-Hückel approximation for weakly charged surfaces one has $\zeta_T = \frac{1}{2}\zeta$ and thus recovers (2) with an additional factor $\frac{1}{4}$.

The remainder of Eq. (27) accounts for permittivity and salinity gradients. The former describes how a permittivity gradient results in a spatially varying electric energy density εE^2 and thus gives rise to an electrostrictive force [73]; according to (25) the fluid in the boundary layer moves to regions of low ε. Here we consider the case where a permittivity gradient arises from a non-uniform temperature [78, 79],

$$\frac{\boldsymbol{\nabla}\varepsilon}{\varepsilon} = -\tau\frac{\boldsymbol{\nabla}T}{T}. \tag{28}$$

The dimensionless temperature coefficient of water is positive; at room temperature it takes the value $\tau = 1.4$. Thus this contribution leads to a quasislip velocity v_B towards the warm; the particle moves to lower temperatures. Finally, the term proportional to $\boldsymbol{\nabla}n_0$ corresponds to Anderson's chemiphoretic contribution [70]. A higher salinity reduces both the surface potential and the Debye length, thus lowering the electric-double layer energy. In this picture, the particle is attracted towards region of higher salt concentration [80].

According to Fig. 4b and Eq. (25) there is a permanent flow of charged liquid along the particle surface. The resulting excess charges of opposite sign at the cold and warm side of the particle are resorbed by diffusion to the bulk; there is a long-range ion current similar to the flow pattern of Fig. 5, but of opposite direction. The above treatment supposes that the convection flow in the double layer is slow as compared to the back-diffusion in the outer region. In the case of strong interaction with the particle surface, the convective charge current in the boundary layer results in an additional polarization, as illustrated in Fig. 6. For slow ion diffusion beyond the double layer, positive and negative excess charges accumulate at opposite sides of the particle and reduce the transport velocity. Following early work by Dukhin and Derjaguin [81], the saturation of the osmotic flow has been worked out for neutral solutes [80], for electrophoresis [82], and for motion driven by a salinity gradient [83, 84]. Thus the linear increase of the electrophoretic mobility $\varepsilon\zeta/\eta$ bends down at sufficiently large surface potentials and shows a maximum where the Dukhin number equals unity [85],

$$\frac{\lambda}{a}e^{e|\zeta|/2k_BT} \sim 1;$$

with $\lambda = 10$ nm and $a = 1$ μm this occurs at $\zeta \sim 200$ mV. For such high values similar modifications are expected for thermophoresis. More generally, one should keep in mind that for highly charged systems, Poisson-Boltzmann mean-field theory ceases to be valid, and correlation effects may become important [86, 87]; at short distances, the continuum picture misses the discrete nature of the surface charges [88].

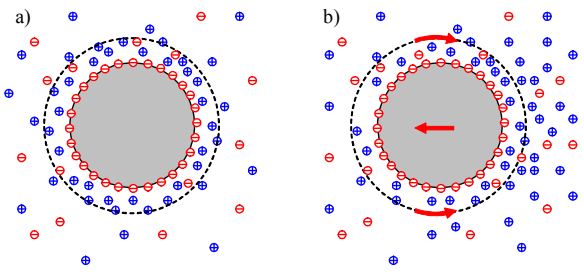

FIG. 6: a) Charged particle with its screening cloud; the dashed line indicates the Debye length. b) Polarization of the electric double layer. An electric field or interface forces drive the charged liquid along the surface to the right; the particle moves in the opposite direction. The surface flow leads to an accumulation of counterions at the right end of the sphere, and to depletion at the left. If back diffusion of the mobile ions is sufficiently rapid, the polarization is weak and hardly affects the transport velocity. For very large surface potentials, i.e., for large Dukhin number, polarization reduces the particle mobility.

D. Non-uniform electrolyte

The transport velocity (27) is given in terms of an electric field and gradients of the parameters T, ε, n_0 of the electrolyte solution. These external fields are not independent of each other, but are related by the thermodynamics and kinetics of the mobile ions. If one such field is applied from outside, the response of the electrolyte will generate companion fields. Such effects occur both in the steady state and in the transient following a temporary change of a system variable.

Consider an electrolyte with monovalent ions of charge $q_i = z_i e$ and densities n_i, with the salinity

$$n_0 = \frac{1}{2}\sum_i n_i.$$

The current of each species,

$$\mathbf{J}_i = -D_i\left(\boldsymbol{\nabla} n_i + n_i\frac{Q_i^*}{k_B T^2}\boldsymbol{\nabla} T - n_i\frac{q_i\mathbf{E}_0}{k_B T}\right), \qquad (29)$$

comprises normal diffusion with the Einstein coefficient D_i, thermal diffusion with the ionic heat of transport Q_i^*, and an electric-field term that remains to be determined [44]. Since the permittivity is sensitive to temperature only, its variation has been absorbed in the heat of transport. Macroscopic charge separation and currents are prohibited by the huge electrostatic energy, implying the relations

$$\sum_i q_i n_i = 0, \quad \sum_i q_i \mathbf{J}_i = 0.$$

Yet a net charge density may occur at the sample boundary, or during the relaxation of an initial non-equilibrium salinity.

As an example, consider a binary electrolyte solution at constant temperature $\boldsymbol{\nabla} T = 0$ but with an externally imposed salt gradient $\boldsymbol{\nabla} n_0$. If the Einstein coefficients $D_\pm$ of positive and negative ions differ, one species diffuses more rapidly than the other. Thus positive and negative ions accumulate in different regions, resulting in polarization and a macroscopic electric field. The latter is readily obtained from the zero-current condition [83],

$$\mathbf{E}_0 = \gamma\frac{k_B T}{e}\frac{\boldsymbol{\nabla} n_0}{n_0}, \qquad (30)$$

where the proportionality constant is given by the normalized difference of the diffusion coefficients

$$\gamma = \frac{D_+ - D_-}{D_+ + D_-}.$$

Inserting in (27) one finds that a salinity gradient gives rise to two velocity contributions,

$$\mathbf{u} = \left(\gamma\frac{\varepsilon\zeta}{\eta}\frac{k_B T}{e} + \frac{\varepsilon\zeta_T^2}{3\eta}\right)\frac{\boldsymbol{\nabla} n_0}{n_0}. \qquad (31)$$

The chemiphoretic one, proportional to ζ_T^2, is always positive, whereas the electrophoretic term $\propto \gamma$ may take both signs. The more the diffusion coefficients of positive and negative ions differ, the larger is the electric-field term. The latter modifies qualitatively the transport properties of common electrolytes; the parameter γ varies from -0.5 for NaOH to $+0.7$ for HCl [83].

E. Thermoelectricity

Now we consider what happens when a finite temperature gradient is applied to an initially uniform electrolyte. According to Eq. (29) the ionic heat of transport Q_i^* creates a current along the thermal gradient and thus induces a non-uniform salt concentration. The present discussion is restricted to the steady state $\mathbf{J}_i = 0$, which is achieved when the diffusion term, proportional to $\boldsymbol{\nabla} n_0$, equilibrates the thermal and electric-field driven currents.

We first consider the salinity n_0. Summing over all ion species and defining the reduced Soret coefficient α of the electrolyte solution by the mean heat of transport

$$\alpha = \sum_i \alpha_i\frac{n_i}{n_0}, \qquad \alpha_i = \frac{Q_i^*}{2k_B T}, \qquad (32)$$

we find the stationary state as

$$\frac{\boldsymbol{\nabla} n_0}{n_0} = -\alpha\frac{\boldsymbol{\nabla} T}{T}. \qquad (33)$$

For a positive heat of transport one has $\alpha > 0$, and the salinity is higher at lower temperature. If Q_i^* takes the same value for all ion species, the non-uniform electrolyte is completely described by Eq. (33) in terms of the salt

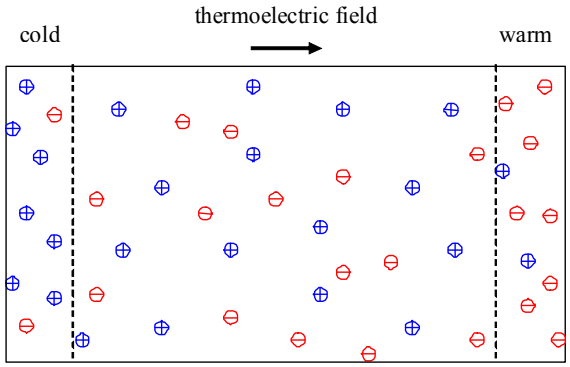

FIG. 7: Macroscopic electric field E_0 arising from a thermal gradient in a binary electrolyte solution. The positive and negative ions accumulate at the opposite sample boundaries and form charged layers that are about one Debye length thick. In the bulk the charge density vanishes and the field E_0 is constant. The situation shown occurs for a positive coefficient $\delta\alpha = \alpha_+ - \alpha_- > 0$, where the cations move to the cold and the anions to the warm; then the thermoelectric field and the temperature gradient point in the same direction.

Soret coefficient α/T. Historically, the Soret effect was discovered by Ludwig for a solution of Na_2SO_4 [24]; Soret did his first measurements on sodium chloride and potassium nitrate [25].

In addition to the overall motion of the dissolved salt there is a relative motion of positive and negative ions. As illustrated by the numbers in Table I, the heats of transport of cations and anions are in general quite different. Thus the thermally driven current is stronger for the species with the larger Q_i^*; this difference in diffusion velocity gives rise to a macroscopic electric field. Fig. 7 shows the accumulation of ions of opposite charge at the hot and cold sample boundaries, and the resulting thermoelectric field. Its steady-state value is obtained from the condition of zero electrical current and zero bulk charge density; following Guthrie et al. [44] we put $\mathbf{J}_i = 0$ and $\rho = 0$ and thus find

$$\mathbf{E}_0 = \delta\alpha \frac{k_B \boldsymbol{\nabla} T}{e}, \tag{34}$$

where the dimensionless coefficient

$$\delta\alpha = \sum_i z_i \alpha_i \frac{n_i}{n_0} \tag{35}$$

is the weighted average of the α_i, with $z_i = \pm 1$ for positive and negative ions. For a binary electrolyte these relations reduce to $\alpha = \alpha_+ + \alpha_-$ and $\delta\alpha = \alpha_+ - \alpha_-$.

The macroscopic field $\mathbf{E}_0$ implies an electrostatic potential difference, or thermopotential, between the cold and hot boundaries of the sample. This thermopotential $\psi_0 \Delta T/T$ is given by the temperature difference ΔT and a constant accounting for the electrolyte properties,

$$\psi_0 = -\delta\alpha \frac{k_B T}{e}. \tag{36}$$

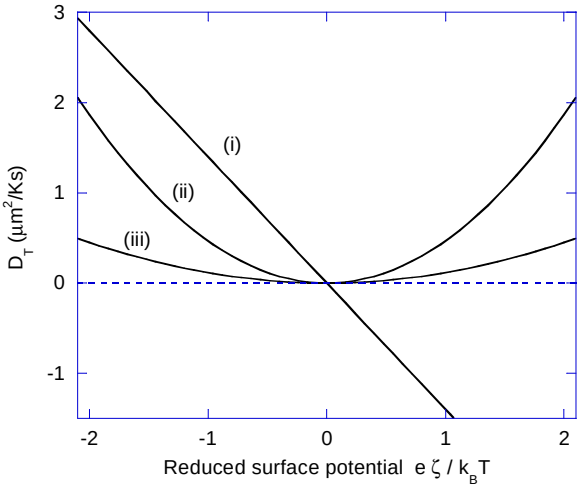

FIG. 8: Magnitude of the contributions to the transport coefficient (37) as a function of the reduced surface potential $e\zeta/k_BT$. (i) The straight line gives the thermoelectric term proportional to $\zeta\psi_0$ for $\delta\alpha = 1$; (ii) gives the term proportional to the square of the surface potential ζ^2; (iii) gives the remainder proportional to $\zeta_T^2 = 8 \ln\cosh(e\zeta/4k_BT)$ with $\alpha = \tau = 1$. For typical values of the surface potential, the first two terms prevail, whereas that $\propto \zeta_T^2$ is of little significance; it is discarded in Eq. (38).

For a binary electrolyte, it is related to the heats of transport through $\psi_0 = (Q_- - Q_+)/2e$. Inserting the relation $\mathbf{E}_0 = -(\psi_0/T)\boldsymbol{\nabla} T$ and the salinity and permittivity gradients (28) and (33), and writing the transport velocity in the form $\mathbf{u} = -D_T \boldsymbol{\nabla} T$, we obtain the thermophoretic mobility

$$D_T = \frac{\varepsilon}{\eta T}\left(\frac{\zeta^2}{3} + \zeta\psi_0 - \zeta_T^2\left(1 - \frac{\alpha+\tau}{3}\right)\right). \tag{37}$$

The surface potential of most experimental systems takes values of a few k_BT/e. In this range, the terms proportional to ζ_T^2 turn out to be of little significance and thus will neglected in the following. Fig. 8 compares the three contributions to D_T as a function of the reduced quantity $e\zeta/k_BT$, for typical values of the parameters α, $\delta\alpha$, and τ.

This means in particular that we discard the salinity

TABLE I: Heat of transport Q_i^* and reduced Soret coefficient α_i at room temperature for dilute systems. The α_i are calculated from Eq. (32), with the values Q_i^* taken from Ref. [89]. These numbers are subject to experimental uncertainty; Ref. [90] gives a signficantly larger value for the Soret coefficient $\alpha_{Cl} = 0.5$ of Cl ions.

Ion	H^+	Li^+	K^+	Na^+	OH^-	Cl^-
Q_i^* (kJ/Mol)	13.3	0.53	2.59	3.46	17.2	0.53
α_i	2.7	0.1	0.5	0.7	3.4	0.1

and permittivity gradients. The resulting coefficient

$$D_T = \frac{\varepsilon\zeta}{\eta T}\left(\frac{\zeta}{3} + \psi_0\right) \tag{38}$$

accounts for two physical mechanisms that were introduced in (2) and (3). The term proportional to the square of the surface potential is closely related to Derjaguin's enthalpy flow [40]; it is always positive and drives the particle towards lower temperatures, whereas the thermoelectric potential ψ_0 may take both signs. For a negatively charged particle $\zeta < 0$, an inverse Soret effect ($D_T < 0$) occurs if $\psi_0 > -\frac{1}{3}\zeta$; this condition is achieved for a sufficiently negative $\delta\alpha$. The straight line (i) of Fig. 8 is calculated with the typical electrolyte coefficient $\delta\alpha = 1$; Table I indicates $\delta\alpha = 0.6$ for NaCl at room temperature. This thermoelectric contribution exceeds the term due to enthalpy flow in the whole range of relevant surface potentials. (Note that k_BT/e corresponds to 26 mV.)

The origin of the field $\mathbf{E}_0$ in (27) is similar to thermoelectricity in metals, where the Seebeck coefficient $S = -\psi_0/T$ is defined as the ratio of induced voltage and temperature difference. With typical values of a few μV/K, the coefficient of metals is much smaller than that of electrolyte solutions; Table II shows that ψ_0/T may attain hundreds of μV/K. The Dufour effect describes the inverse phenomenon, where a concentration gradient is accompanied by a heat flow and thus leads to a nonuniform temperature [1]. Contrary to gases where both Seebeck and Dufour coefficients are relevant, the latter is weak in liquids, mainly because of the large heat capacity.

In dilute electrolyte solutions, the ionic heat of transport Q^* arises from specific hydration effects [91]; at salt concentrations beyond a few mMol/l electrostatic interactions become important and result in intricate dependencies on temperature and salinity [28–30]; such effects are neglected here, where the coefficients are taken as constants. According to the heats of transport given in Table I, protons and hydroxide ions are most efficient sources of the thermoelectric field; thus in weak electrolyte solutions, the pH value determines the magnitude and the sign of the thermophoretic transport coefficient D_T.

The effect of adding NaCl or LiCl to a low-acidity buffer solution is illustrated in Fig. 9. The points present experimental data from Ref. [5] for 26-nm polystyrene beads in a CAPS (cyclohexylamino-propanesulfonic acid-NaOH) buffered electrolyte. Since the Soret parameters

TABLE II: Thermopotential parameter ψ_0 and Seebeck coefficient $S = -\psi_0/T$ for several electrolytes at room temperature, as calculated from the numbers of Table I.

Electrolyte	NaCl	NaOH	HCl	KCl
$\delta\alpha$	0.6	−2.7	2.6	0.4
ψ_0 (mV)	−16	70	−68	−10
S (μV/K)	50	−210	205	30

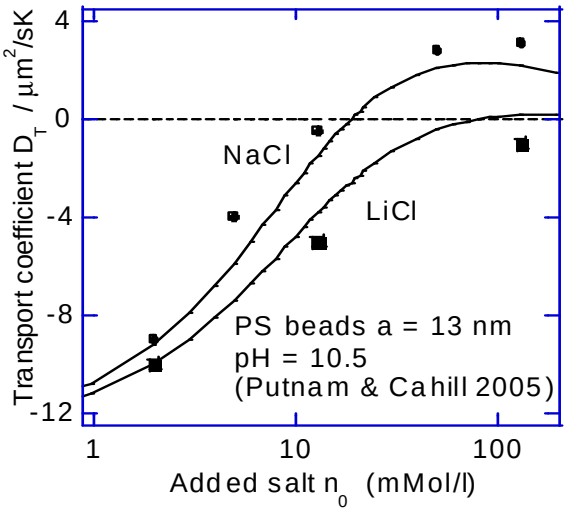

FIG. 9: Thermophoretic mobility at large pH.as a function of added salt concentration (NaCl or LiCl). The data points are taken from Fig. 5a and 5b of Ref. [5]; they are obtained for polystyrene beads of radius $a = 13$ nm in a CAPS buffered electrolyte solution at fixed pH. The curves are calculated from Eq. (37) with the ionic Soret coefficients of Table 1 for Na or Li, Cl, and OH, assuming a constant charge density $\sigma = -0.12$ nm^{-2}. The hydroxide concentration $n_{\rm OH} = 12$ mMol/l corresponds to a pH value of about 10.5. Reprinted from Ref. [42].

for the buffer molecules are not known, only Na, Li, Cl, OH are taken into account, with the values of Table I. The pH value 10.3 corresponds to a hydroxide concentration of about 12 mM/l. Thus at low salinity, the electrolyte is a NaOH solution; the strong thermodiffusion of OH ions to low temperatures induces a thermoelectric field which in turn drives the negatively charged PS beads to the warm. Adding salt weakens this effect through the decreasing relative weight of $\delta\alpha_{\rm NaOH}$ in the coefficient

$$\delta\alpha = \frac{n_{\rm NaOH}\ \delta\alpha_{\rm NaOH} + n_0\ \delta\alpha_0}{n_{\rm NaOH} + n_0}. \tag{39}$$

For $n_0 \gg n_{\rm NaOH}$, the pH value becomes irrelevant for the thermophoretic mobility; since NaCl gives rise to a rather weak thermoelectric effect, colloid transport arises from the double-layer energy, i.e., the term $\propto \zeta^2$ in (38). Replacing the CAPS buffer with citric acid or using tetraethylammonium hydroxide as salt, changes the behavior of D_T, indicating that these molecules contribute significantly to the thermoelectric field.

The importance of the electrolyte composition is highlighted by changing the relative weight of a given ion at constant salinity. In Fig. 10 we plot D_T for a negatively charged particle in a 20 mMol/l $\mathrm{NaCl}_{1-x}\mathrm{OH}_x$ solution as a function of the relative hydroxide content x. Since the thermoelectric effect is weak in a pure NaCl solution, at $x = 0$ the mobility takes a rather small positive value

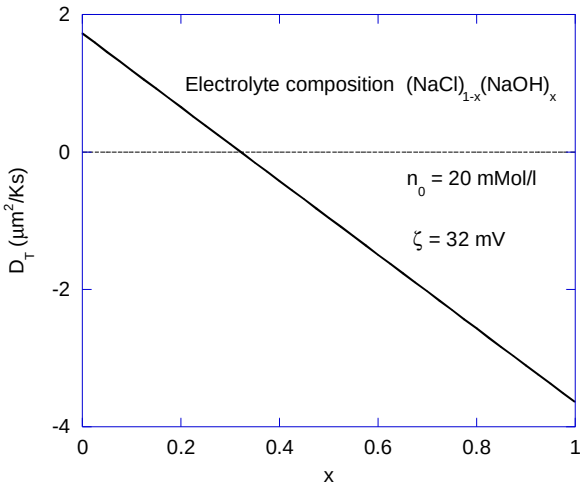

FIG. 10: Thermophoretic mobility as a function of the electrolyte composition. At constant salinity $n_0 = 20$ mMol/l, the partial concentrations of NaOH and NaCl are given by xn_0 and $(1-x)n_0$, respectively. The surface potential of 32 mV corresponds to $e\zeta/k_BT = -1.3$.

$D_T = 1.7\mu\text{m}^2/\text{Ks}$. The macroscopic field E_0 strongly increases with the OH concentration, and results in a change of sign at $x = 0.3$. This means that 6 mMol/l NaOH are sufficient to drive the particle to the warm; in a pure NaOH solution, the mobility attains the value $D_T = -3.6\text{m}^2/\text{Ks}$, which is more than twice as large as in NaCl and of opposite sign. The linear variation with x and the change of sign are confirmed by a very recent experiment on SDS micelles in a composite electrolyte [92].

So far we have discussed a one-dimensional geometry where the temperature gradient and the thermoelectric field are constant in space. Experimental techniques based on optical gratings and thermal lensing [12], however, create spatially varying temperature gradients. Though the above analysis is expected to apply to any geometry, a caveat is in order concerning the definition of the "bulk region" where Eq. (34) applies. This is particularly relevant for single-particle tracking techniques in the vicinity of a heated spot in microchannels of thin water films [6].

F. Collective effects

In dilute suspensions, the thermophoretic mobility D_T and the diffusion coefficient D are independent of the colloidal volume fraction, and so is the Soret coefficient S_T. A different behavior, however, was observed in a number of experiments. For 3-nanometer SDS micelles at volume fractions ϕ ranging from 0.1% to 2%, Piazza and Guarino found the measured Soret coefficient to vary as $S_T \propto 1/(1+k_s\phi)$, and the coefficient k_s to be proportional to the inverse salinity [4].

This dependence of S_T on the SDS concentration has been related to particle-particle interactions; the corresponding expansion for the diffusion coefficient reads at linear order

$$D = \frac{k_BT}{6\pi\eta a}\,(1+2B\phi)\,. \tag{40}$$

For a screened electrostatic repulsion, B indeed varies with the inverse salinity [4, 93]. Both features agree well with the experimental observation for the Soret coefficient $S_T = D_T/D$, and suggest that collective diffusion is at the origin of the observed concentration dependence. This view is confirmed by comparing data from Refs. [94, 95] on suspensions of 12 nm Ludox particles at volume fractions 0.1%, 0.5%, and 1.1%: At low salinity the variation of the Soret coefficient with ϕ is, at least qualitatively, accounted for by Eq. (40).

A more complex picture arises from a recent experiment on silica beads in an aqueous sulpho-rhodamine B solution [96]. An independent measurement of the functions $D(\phi)$ and $S_T(\phi)$ shows that their concentration dependencies do not cancel, resulting in a significant variation of the thermophoretic mobility $D_T = S_TD$. In the range of volume fractions between 0 and 5%, the diffusion coefficient D almost triples its value, whereas D_T and S_T are reduced by factors of 2 and 5, respectively. At higher densities $\phi > 0.1$ all quantities seem to saturate.

The linear inital increase of the data of Ref. [96] with the collective diffusion coefficient D, gives a dimensionless virial coefficient $2B \approx 35$. A theoretical estimate $2B = (r_0/a)^3$ is obtained from the excluded volume due to electrostatic repulsion $r_0 = 2a + \chi\lambda$, with the radius of silica beads $a = 35$ nm, the Debye length λ, and a numerical factor χ [93]. Treating the 30 μM/l sulpho-rhodamine B solution as a monovalent electrolyte with a Debye length of about 50 nm, one finds that the screened electrostatic repulsion leads a virial coefficient comparable to the measured value. This does not explain the flattening of $D(\phi)$ at $\phi > 0.1$ nor the variation of the thermophoretic mobility D_T.

Besides the "thermodynamic" contribution $2B\phi$, the virial coefficient for the diffusion coefficient $(2B + K_2)\phi$ contains a "hydrodynamic" term K_2. For hard spheres both are of comparable magnitude but opposite sign, $2B = 8$ and $K_2 = -6.5$ [77], whereas in the case of the charged silica beads considered here, the thermodynamic term is by far dominant. Note that the main part (-5.5) of the numerical value of K_2 is due to backflow.

Cooperative effects on the thermophoretic mobility D_T are less well understood. A thermally driven particle gives rise to the "dipolar" velocity field $\mathbf{v} \sim 1/r^3$ shown in Fig. 5 and thus does not drag the surrounding fluid; as discussed in Sect. IV below, this flow pattern implies that there is no backflow. Thus one expects the hydrodynamic coefficient K_2 of D_T to be smaller than the above value of D. At volume fractions $\phi < 5\%$, these corrections cannot explain the observed effect on D_T. Little is

known on how pair interactions affect the mobility D_T. In a purely thermostatic approach, Dhont evaluated D and D_T as derivatives of a generalized non-equilibrium partition function [97]. In this way he reproduced the known virial expansion for the diffusion coefficient. Yet the thermophoretic mobility takes the form $D_T = D/T$ and thus is proportional to the inverse particle radius.

In conclusion, the experimental findings of Ref. [96] strongly suggests that thermophoresis in semidilute suspensions is subject to significant collective effects, which are at present rather poorly understood. It would be interesting to determine whether the silica beads investigated in [96] are an exception, or whether D_T of particle suspensions in general varies with volume fraction. An even stronger hint on the existence of collective effects is given by the molecular-weight dependence of the mobility D_T of polyelectrolytes and DNA, as discussed in Sect. IV E.

G. Temperature dependence

The thermophoretic mobility of colloidal suspensions shows an intriguing temperature dependence. For proteins, DNA, SDS micelles, and polystyrene beads, several authors report a linear increase with temperature; D_T is negative at low T and changes sign between 5° and 25° C [6, 32, 33]. In view of Eq. (38) we note that the permittivity ε and the surface potential ζ depend only weakly on temperature; the variation of the viscosity, though quite significant, cannot explain the change of sign of D_T.

Piazza and co-workers [32, 33, 67] found that the temperature dependence of the Soret coefficient is well described by the formula

$$S_T = S_T^\infty \left(1 - e^{\frac{T^*-T}{T_0}}\right). \tag{41}$$

This expression is negative at low T and changes sign at T^*. With experimentally relevant parameters, one finds a linear variation below room temperature, $S_T = S_T^\infty(T - T^*)T_0$, and a much weaker increase at higher T. This rather universal behavior shown by various macromolecular and particle suspensions strongly suggests a common origin. Its physical origin is not clear at present.

Here we discuss the thermoelectric effect as a possible mechanism for the temperature dependence. The Soret coefficient of binary electrolytes shows intricate dependencies on ion size, salinity, and temperature [28, 30], that arise from a superposition of electrostatic interactions, thermal expansion, and hydration effects. Measurements on 0.5 M/l NaCl solution give a constant slope

$$\frac{d\alpha}{dT} = 0.03\ \mathrm{K}^{-1}$$

between 0 and 25 °C, and smaller values at higher temperatures [28]. Regarding the behavior at lower salinity, available experiments indicate a monotonic increase of α with temperature. An irregular feature occurs for NaCl and KCl at 100 mM/l [28, 30], where the coefficient α as a function of salinity shows a sharp dip towards negative values. A similar dip has been observed for the Soret coefficient S_T of lysozyme protein: the value measured at $n_0 = 100$ mMol/l is significantly smaller than those at 20 and 400 mMol/l [32]. With the ionic heats of transport of Table I, one finds $\delta\alpha = 0.6$ for NaCl solution at room temperature.

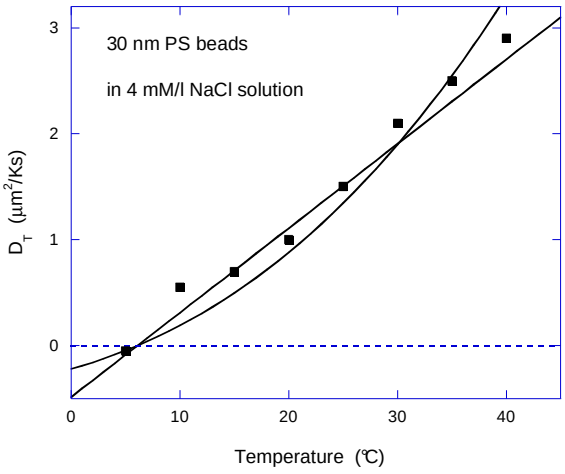

FIG. 11: Temperature dependence of the thermophoretic mobility of polystryene beads. The full symbols are data measured by Iacopini et al. [33]. The curves represents Eq. (38) with the the Debye length $\lambda = 5$ nm and the number density of elementary surface charges $\sigma = -0.05$ nm^{-2}; the latter value is slightly larger than -0.04 nm^{-2} given in Ref. [33]. The temperature dependence of the straight line arises from the thermoelectric coefficient $\delta\alpha$; the second curve accounts moreover for the variation of the viscosity, as explained in the main text. (Reprinted with permission from Ref. [98]. Copyright 2009 American Chemical Society.)

In the absence of data on the temperature dependence of the thermoelectric coefficient $\delta\alpha$, we tentatively assume a linear behavior, similar to that of the Soret coefficient α. The straight line in Fig. 11 is calculated from Eq. (38) with

$$\delta\alpha(T) = 0.8 + \frac{0.025}{\mathrm{K}}(T - 298\ \mathrm{K}). \tag{42}$$

Its parameters roughly correspond to the measured value at 25 °C given in Table I, and to the T-dependence of α. Thus Eq. (42) crucially relies on the assumption that α and $\delta\alpha$ have a similar temperature dependence. In terms of the ionic transport quantities introduced in Eq. (32), this means that Q^*_{Na} and Q^*_{Cl} would follow the same law as a function of T.

We briefly return to the temperature variation of the viscosity η. In the range between 10 °C and 40 °C, the viscosity decreases by about 50% from 1.3×10^{-3} Pa·s to 0.65×10^{-3} Pa·s [99]; this reduction corresponds to a logarithmic derivative $d\ln\eta/dT \sim -0.02$ K^{-1}. The

straight line in Fig. 4 is calculated with the constant value η_0 at 30 °C. The second curve is calculated with the temperature-dependent viscosity data $\eta(T)$ from Ref. [99]. For the present discussion, the difference between the two curves is of little significance.

The data reported by Iacopini et al. for sodium dodecylsulfate (SDS) micelles and sodium polystyrenesulfonate (NaPSS), are almost identical to those for polystyrene beads shown in Fig. 11. In all cases, D_T changes sign at $T^* \approx 5°$ C, increases linearly with temperature, and attains values between 3 and 5 μm^2/Ks above 30° C; the same behavior is found for the peptide β-lactoglobulin and for DNA, with a change of sign at 20° C [33]. The results on polystyrene beads and DNA are confirmed by Ref. [6]. These colloids are negatively charged ($\zeta < 0$) and are soluted in a NaCl electrolyte.

In view of the good agreement of the data with Eq. (42) it is tempting to conclude that the temperature dependence arises from that of the thermoelectric coefficient $\delta\alpha$ of the NaCl solution. Yet experimental findings on the positively charged peptide poly-lysine do not support this picture: The measured mobility D_T increases with temperature [33, 100], similar to that shown in Fig. 11, whereas from the above discussion one would expect a negative slope $dD_T/dT < 0$ for a positive surface potential ($\zeta > 0$) [101]. At present it is not clear whether this discrepancy is due to hydrophobic interactions or to a more subtle coupling of the thermoelectric field. Definitively settling this question would require an experimental study of the electrolyte coefficient $\delta\alpha(T)$.

H. Slip boundary condition

Our discussion so far relies on Stokes boundary conditions $v_x|_{z=0} = 0$ for the fluid motion near the particle; in a microscopic picture this means that the first layer of solvent molecules sticks to the solid surface. Though this condition is verified on a macroscopic level, alternatives have been debated since the early days of fluid mechanics. Navier proposed that a sheared fluid could slip along the surface, with the velocity jump v_0 being proportional to the applied shear stress Σ_0,

$$\eta v_0 = b\Sigma_0, \tag{43}$$

where the material specific constant b has the dimension of a length. Fig. 12 shows the resulting velocity profile through the boundary layer and illustrates the meaning of the parameter b.

A number of experiments indicate the occurrence of hydrodynamic slippage, mainly under non-wetting conditions; recent reviews are given by Refs. [102, 103]. Simulations of the molecular dynamics at a charged interface related the slip length to van der Waals force parameters of the non-wetting fluid and to ion-specific interactions [104]. These simulations show that continuum hydrodynamics provide a good description of the fluid motion

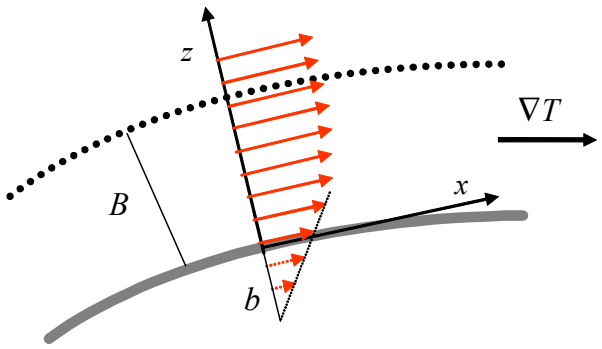

FIG. 12: Schematic view of the fluid velocity field in the boundary layer close to a particle of radius a, after Ref. [105]. The external field acting on the electric double layer accelerates the charged fluid with respect to the solid. A finite surface velocity v_0 arises from hydrodynamic slip in a molecular layer (thick grey line); the slip length b is defined as the distance where the linear velocity profile would vanish. At a distance B, well beyond the electric double layer, the fluid attains the boundary velocity v_B. (Reprinted with permission from Ref. [106].)

even on the scale of nanometers, and that slip occurring in a few molecular layers may significantly accelerate externally driven transport, such as the flow in a microchannel [105].

Following Ref. [106] and proceeding as in Sect. II A, we derive the motion of a particle with slip boundary conditions. We write the fluid velocity and stress at $z = B$ as

$$v_B = v_0 + \Delta v, \qquad \Sigma_B = \Sigma_0 - \Delta\Sigma, \tag{44}$$

where the variation through the boundary is given by the quantities

$$\Delta v = \frac{1}{\eta}\int_0^B dz z\tilde{f}_x, \qquad \Delta\Sigma = \int_0^B dz\tilde{f}_x, \tag{45}$$

with the shorthand notation $\tilde{f}_x = f_x - dP/dx$. Thus the boundary velocity v_B is the sum of an intrinsic slip contribution v_0 and the change through the boundary layer Δv, sometimes referred to as apparent slip [70]. The former occurs if the fluid molecules do not fully adhere to the solid, whereas the latter is due to the forces exerted by the surface on the nearby fluid.

The above equations are closed by the stress-velocity relation outside the boundary layer. Simplifying for $B \ll a$ one obtains from Eq. (17)

$$a\Sigma_B = -2\eta v_B. \tag{46}$$

Solving the relations (43)-(46) one finds the boundary velocity v_B as a function of Navier's slip length,

$$v_B = \frac{\Delta v + b\Delta\Sigma/\eta}{1 + 2b/a}. \tag{47}$$

The velocity and stress increments Δv and $\Delta\Sigma$ do not depend on the particle size. For Stokes boundary conditions ($b = 0$) one recovers $v_B = \Delta v$, and the boundary velocity v_B is independent of the radius a. The opposite limit $b \to \infty$ leads to $v_B = \frac{1}{2}a\Delta\Sigma/\eta$, which varies linearly with a.

The boundary velocity comprises two contribution of different physical origin. The first term involves Anderson's "quasislip" velocity Δv, which arises from osmotic flow due to interfacial forces; this velocity occurs on a length scale determined by the range of interaction, e.g., the Debye length in the case of electrokinetic phenomena. The second contribution, proportional to the change of stress $\Delta\Sigma$, corresponds to slip in the sense of the Navier relation (43); in the framework of continuum hydrodynamics, there is no associated length scale, in a microscopic picture slippage is related to the weak adhesion of the first molecular layers to the particle, as occurring for water at a hydrophobic surface [104]. Some aspects of hydrodynamic slippage at a solid-fluid interface are similar to the flow on a gas bubble in a viscous liquid [107, 108].

As an example, we evaluate Eq. (47) for electroosmotic flow, where a charged particle with its screening cloud is subject to an external electric field E_0. Straightforward integration gives $\Delta\Sigma = -\sigma E_0$ and $\Delta v = -\varepsilon\zeta E_0/\eta$, where ζ and σ are the surface potential and charge density [70]. Thus we find the boundary velocity v_B and the electrophoretic mobility $\mu = -v_B/E_0$,

$$\mu = \frac{1}{\eta}\frac{\varepsilon\zeta + \sigma b}{1 + 2b/a}. \tag{48}$$

For $b = 0$ we recover the Helmholtz-Smoluchowski expression $\mu = \varepsilon\zeta/\eta$, whereas in the opposite limit $b \to \infty$, the mobility simplifies to $\mu = a\sigma/2\eta$. In the weak-coupling limit, the surface potential reads as $\zeta = \lambda\sigma/\varepsilon$; for moderate slip length $b \ll a$, this results in the correction factor $\mu = (1 + b/\lambda)\varepsilon\zeta/\eta$ given previously in [109]. The case of large Dukhin number is discussed in [110].

A physical picture for the slip-enhanced mobility is obtained in terms of the range of the shear stress σE, that is exerted by an electric field on the surface of charge density σ. For $b = 0$ the stress occurs over the width λ of the double layer, resulting in the relation for the velocity $\eta u/\lambda \sim \sigma E$, as illustrated in Fig. 4b. A finite slip b length spreads the stress over a larger distance; from Fig. 12 one finds $\eta u/b \sim \sigma E$, and the particle velocity augments accordingly. This effect saturates if b exceeds the radius a; then the stress operates over a distance of the order of the particle size, $\eta u/a \sim \sigma E$.

Now we discuss how slip boundary conditions affect motion driven by chemical and thermal gradients. For the sake of notational simplicity, we consider the weak-coupling case only, where the surface potential is small, $e\zeta < k_B T$. General results for strong coupling are obtained by inserting the force (22) in Eq. (45). In Debye-Hückel approximation one has $\psi = \zeta e^{-z/\lambda}$ and $\zeta_T = \frac{1}{2}\zeta$. Integrating Eqs. (32) and (45) results in the transport velocity

$$\mathbf{u} = \frac{\varepsilon\zeta^2}{12\eta}\left(\frac{\boldsymbol{\nabla}\varepsilon}{\varepsilon} + \frac{\boldsymbol{\nabla}n_0}{n_0} - \frac{\boldsymbol{\nabla}T}{T}\right)\frac{1 + 2b/\lambda}{1 + 2b/a}. \tag{49}$$

Note that this result has been obtained in boundary layer approximation, which is valid for $\lambda \ll a$ only. The dependence on the Navier slip length b is given by the last factor. A discussion of the strong-coupling case in terms of the Dukhin number is given in Ref. [110].

For $b = 0$ we recover Ruckenstein's expression for thermally driven transport, which is proportional to the square of the surface potential and opposite to the temperature gradient [2]. Moderate values of b enhance the velocity by $1+2b/\lambda$. In comparison to the electrophoretic velocity at low surface potential,

$$\mathbf{u} = \frac{\varepsilon\zeta\mathbf{E}_0}{\eta}\frac{1 + b/\lambda}{1 + 2b/a},$$

Eq. (49) shows an additional factor of 2 in the numerator, which is related to the quadratic dependence on ζ. For $b \gg a$ the enhancement factor in (49) reduces to a/λ and no longer depends on the slip length; in this range the transport velocity is proportional to the particle size [12, 72]. Numerical studies of non-wetting interfaces suggest that b takes values of less than ten nanometers; from Eqs. (48) and (49) one expects a rather moderate increase of the transport velocity.

I. Size dependence

The hydrodynamic and electrostatic treatment of colloidal particles presented so far, relies on the boundary layer approximation, which is valid for short-ranged solute-solvent forces. In this limit the thermophoretic mobility does not depend on the particle size [40, 70],

$$D_T \quad \text{constant} \quad (a \gg \lambda). \tag{50}$$

The essential argument is illustrated in Fig. 4, showing how the boundary velocity arises from the local balance of interfacial forces and viscous stress and thus is insensitive to the particle radius. A similar relation has been known for a long time for electrophoresis [111] and for motion driven by chemical gradients [70]. Morrison has shown this statement to hold true for bodies of any shape, as long as the curvature radius is large compared to the range of the interface forces [112]. As two exceptions to the rule (50), we note hydrodynamic slippage on non-wetting surface, and liquid droplets without or with weakly adsorbing surfactants; these cases are discussed in Sects. II H and VI D, respectively. Contrary to D_T, the diffusion coefficient

$$D = \frac{k_B T}{6\pi\eta a} \tag{51}$$

is proportional to the inverse particle radius, resulting in a linear variation of the Soret coefficient $S_T = D_T/D$.

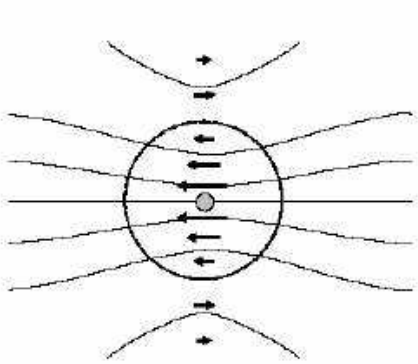

FIG. 13: Schematic view of a charged particle of radius a, and its screening cloud with Debye length $\lambda \gg a$. The arrows indicate the fluid velocity field. At distances within one Debye length, the fluid is dragged by the moving particle to the left. At larger distances, the velocity field is described by (23); close to the midplane it is opposite to the particle motion. (Reprinted from Ref. [115] with permission of the European Physical Journal EPJ E.)

Most experiments on suspended particles and AOT-water-oil emulsion droplets [15, 67, 113, 114] confirm the relation (50); yet note the linear increase of $D_T \propto a$ observed in [6]. For a recent discussion of experimental data on the size dependence see Ref. [67].

Here we address the opposite limit where the particle is smaller than the characteristic length scale of the forces. For example, in a weak electrolyte the Debye length takes values of hundreds of nanometers and may by far exceed the size of nanoparticles or micelles. The small-particle limit $a \ll \lambda$ rather generally applies to molecular ions. For long-ranged forces, the pressure gradient in the Stokes equation is negligible and the solute velocity can be evaluated in the Hückel limit

$$\mathbf{u} = \frac{\mathbf{F}}{6\pi\eta a} \qquad (a \ll \lambda), \tag{52}$$

where the particle-fluid interaction is treated like an external field $\mathbf{F}$. The latter is given by the integral of the total force density (22) exerted by the particle on the surrounding fluid,

$$\mathbf{F} = -\int dV \mathbf{f}. \tag{53}$$

The flow pattern in the vicinity of the particle is indicated in Fig. 13; within one Debye length one finds $\mathbf{v} \sim 1/r$, whereas at larger distances one recovers the variation $\mathbf{v} \sim 1/r^3$ of Eq. (17); for a detailed discussion see [115].

In physical terms, the Hückel limit relies on the wide spreading of counterions and the smooth variation of the viscous stress in the diffuse layer. Thus the hydrodynamic equations reduce to the Stokes drag of a particle of charge q in an electric field $\mathbf{E}_{ext}$. Its velocity is given by Eq. (52) with $\mathbf{F} = q\mathbf{E}_{ext}$, and the electrophoretic mobility by $\mu = q/6\pi\eta a$. Inserting the surface potential of weakly charged particles, $\zeta = \lambda q/4\pi\varepsilon a^2$, one finds that the mobility of small particles, $\mu = \frac{2}{3}\varepsilon\zeta/\eta$, is by a factor $\frac{2}{3}$ smaller than the Helmholtz-Smoluchowski expression $\varepsilon\zeta/\eta$ [77].

Regarding the thermophoretic mobility the argument is less straightforward. Integrating the force $\mathbf{F}$ due to thermoosmotic flow, expanding in powers of a/λ, and truncating at leading terms, Morthomas found that D_T is given by two terms [115]

$$D_T = \frac{\varepsilon\zeta}{\eta T}\left(\frac{\tau}{3}\zeta + \frac{2}{3}\psi_0\right) \qquad (a \ll \lambda), \tag{54}$$

the first of which arises from the permittivity gradient in a non-uniform temperature and the second one accounts for the thermoelectric field. Since the temperature coefficient $\tau = -(T/\varepsilon)d\varepsilon/dT$ is positive and rather close to unity, $\tau \approx 1.4$ at room temperature, the mobility D_T differs little from the expression for large particles, Eq. (38). Thus the discussion of large colloidal particles in Sect. II applies equally well to small solutes. There is a strictly positive contribution proportional to the square of the surface potential, whereas the thermoelectric effect may drive the solute to the cold or the warm, depending on the relative sign and magnitude of ζ and ψ_0. The size dependence of D_T arises from the surface potential which reads in Debye-Hückel approximation

$$\zeta = \frac{q\lambda}{4\pi\varepsilon a(a+\lambda)}.$$

For $a \ll \lambda$ this simplifies to $\zeta = ae\sigma/\varepsilon$, with the surface charge density $e\sigma = q/4\pi a^2$.

It turns out instructive to compare Eq. (54) with a model where the force acting on a particle is calculated as the gradient of the charging energy, that is, of the work required for accumulating a charge q from infinity onto the particle surface, $U = \frac{1}{2}q\zeta$ [93, 116–118]. The gradient has been evaluated by Dhont et al. [117]; to leading order in the small parameter a/λ, the result for the effective force $\mathbf{F}_{\rm eff} = -\boldsymbol{\nabla}U$ reads in our notation

$$\mathbf{F}_{\rm eff} = -2\pi\varepsilon\zeta^2\tau\frac{\boldsymbol{\nabla}T}{T}.$$

Since there is no external field acting on the suspended particle, $\mathbf{F}_{\rm eff}$ describes the force exerted by the charged diffuse layer. Inserting this expression in (52) one finds that the resulting expression for D_T is identical to the first term of (54). Moreover, the Soret coefficient $S_T = D_T/D$ can be written as the temperature derivative of the charging energy,

$$S_T = \frac{dU}{dT} = 2\pi a\frac{\varepsilon\zeta^2}{k_B T^2} \qquad (a \ll \lambda). \tag{55}$$

Thus for small particles the effective-force approach provides the correct expression for the contribution proportional to ζ^2. This is related to the fact that in the Hückel

limit (52) the viscous effects are accounted for by the Stokes mobility factor. There are two sources for the size-dependence discussed in [117]: the explicit variation with a arising from the diffusion coefficient, and that of the surface potential.

III. DISPERSION AND DEPLETION FORCES

A. Colloid-polymer mixtures

Adding polymers to a colloidal suspension affects both its phase behavior and transport properties [119, 120]. Here we consider thermally driven depletion forces in the "colloid limit", where the particle is larger than the gyration radius of the added polymer. This situation is illustrated in Fig. 2a.

We start from the general description of a colloidal particle interacting with a molecular solute. As pointed out by Derjaguin [121] and reviewed by Anderson [70], driven transport is significantly enhanced by accumulation of the solute in the boundary layer. The interaction potential φ between the particle and the solute molecules results in an excess pressure

$$P = ck_BT(e^{-\varphi/k_BT} - 1).$$

Since dispersion force have no lateral component, $f_x = 0$, the integrand of Eq. (15) is given by the derivative dP/dx. This pressure gradient maintains a flow along the particle surface. Noting that only the potential φ depends on the vertical coordinate z, one obtains the quasi-slip velocity

$$v_B = -\frac{1}{\eta}\frac{d}{dx}ck_BT\int_0^\infty dzz\left(e^{-\varphi/k_BT} - 1\right). \qquad (56)$$

The case of an externally applied solute gradient ∇c and constant temperature corresponds to diffusiophoresis [70]. For an attractive interaction one finds $v_B < 0$, that is, the particle is driven towards higher solute concentration ($u > 0$). In the case of strong attraction and high solute density, advection in the boundary layer is limited by diffusion in the nearby fluid, requiring a more detailed analysis [80].

Depletion forces arise from the reduction of the translational entropy due to the finite size. In the above Eq. (56) depletion is accounted for by an infinite repulsive potential for distances shorter than R; with $\varphi = \infty$ for $z < R$ and $\varphi = 0$ for $z > R$, the integral in (56) takes the value $-\frac{1}{2}R^2$. Thus the colloidal particle moves at a velocity

$$\mathbf{u} = -\frac{1}{3\eta}\boldsymbol{\nabla}\left(ck_BTR^2\right). \qquad (57)$$

Sano and co-workers realized such a stationary concentration gradient by a non-uniform temperature [15]. In their experiment shown in Fig. 14, a laser locally heats a colloid-polymer mixture, consisting of charged polystyrene particles of radius $a = 50$ nm and neutral poly-ethylene-glycol (PEG) of molecular weight $M_w = 7500$. The size of an ethylene unit does not exceed a few Å, and each chain is made of $N = 13$ repeat units; the gyration radius R is much smaller than the particle size, thus justifying the boundary layer approximation in (56).

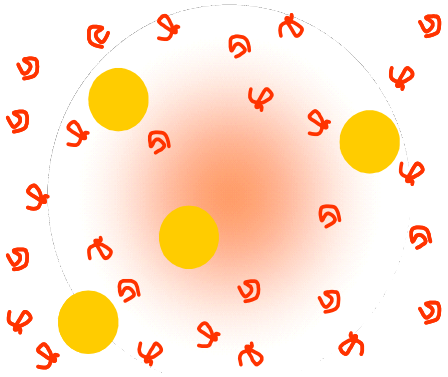

FIG. 14: Schematic view of the non-uniform colloid-polymer mixture studied in Ref. [15]. Laser heating increases the temperature in the center. Because of their positive Soret coefficient, the polymers diffuse to the colder outside region. Their concentration gradient exerts a depletion force on the colloidal particles, which accumulate in the heated spot.

The authors of Ref. [15] discard the variation of the gyration radius and replace the gradient in (57) with $R^2\boldsymbol{\nabla}(cT)$. Under the assumption of a temperature-independent Soret coefficient S_T^m, the non-uniform polymer concentration reads as

$$c(\mathbf{r}) = c_0 e^{-S_T^m \Delta T(\mathbf{r})}. \qquad (58)$$

(A detailed discussion of polymer solutions is given in Sect. IV below.) Inserting the gradient $\boldsymbol{\nabla}c = -cS_T^m\boldsymbol{\nabla}T$ gives the transport velocity of the colloidal particles

$$\mathbf{u} = -\left(D_T^0 - \frac{k_B}{3\eta}R^2c(TS_T^m - 1)\right)\boldsymbol{\nabla}T, \qquad (59)$$

where the first term describes the effect of the thermal gradient on the electric double layer and the second one the depletion force exerted by the polymer solution. The number density of colloidal particles is given by Eq. (11), with the Soret coefficient

$$S_T = S_T^0 - 2\pi cR^2a(S_T^m - 1/T). \qquad (60)$$

Fig. 15 shows the relative colloid density n/n_0 as a function of the temperature increment ΔT, for different weight fractions of polymer content.

For $c = 0$ the depletion force vanishes and the Soret motion is described by the electric double-layer forces accounted for by Eq. (38). The reduction of $n(\mathbf{r})$ in the heated zone means that the colloidal particles are driven towards the cold and that the bare Soret coefficient is

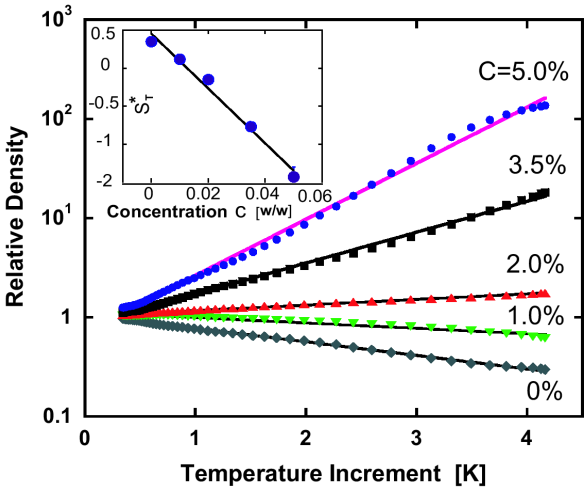

FIG. 15: Reduced colloidal density n/n_0 in the heated spot, as a function of the temperature increment and for several values of the polymer concentration c. The particle radius is $a = 50$ nm. Figure by courtesy of M. Sano. (Reprinted with permission from Ref. [15]. Copyright 2009 American Physical Society.)

positive. Multiplying (38) with the Einstein coefficient one finds

$$S_T^0 = 2\pi a \frac{\varepsilon\zeta(\zeta + 3\psi_0)}{k_B T^2}.$$

The measured value $S_T^0 = 0.35\ \mathrm{K}^{-1}$ corresponds to previous findings for charged polystyrene particles. The two terms in the numerator are expected to be of comparable magnitude; we note that the numerical value of S_T^0 is well reproduced with a surface potential ζ of about 45 mV and $\psi_0 = 0$.

Adding a small amount of polymer reduces the Soret coefficient according to Eq. (60), as shown by the curve for 1% PEG in Fig. 15. At higher concentrations depletion forces overcome the electrostatic mechanism; then the effective value S_T is negative and the colloidal particles accumulate in the heated zone. A temperature increment of 4 K and a polymer volume fraction of 5% enhance the colloidal density by a factor of about 200.

Thus increasing the polymer concentration switches the colloidal Soret effect from thermophobic ($S_T > 0$) to thermophilic behavior ($S_T < 0$). Depletion forces are more efficient for longer polymers; the dependence of the polymer Soret coefficient on the gyration radius given in Eq. (72) below, $S_T^{(m)} \propto R$, leads to

$$S_T - S_T^0 \propto acR^3. \tag{61}$$

This scaling is valid for dilute solutions and as long as the gyration radius is small compared to the particle radius. The linear decrease of S_T^* with polymer concentration is confirmed by the inset of Fig. 15. Regarding the size dependence, the experiments on particles of $a = 50$ and 100 nm confirm the linear law in (61).

The straight lines in Fig. 15 are calculated from Eq. (60) with a polymer Soret parameter $S_T^m = 0.056\ \mathrm{K}^{-1}$ [8], and a gyration radius $R = 5$ nm; the latter corresponds to a Kuhn length of about 3 ethylene units. Finally we discuss S_T^m in view of Eq. (72) derived below: The measured value of S_T^m is met with the definition of the Einstein coefficient (68), the expansivity $\beta = 0.2 \times 10^{-3}\ \mathrm{K}^{-1}$, the radius of a water molecule $d_0 = 1$ Å, and the Hamaker constant $H = 5.5 \times 10^{-20}$ J.

B. Non-uniform solvent

Here we discuss thermophoresis of an uncharged spherical particle of radius a in a non-uniform solvent, as illustrated in Fig. 2. Dispersion forces decay rapidly with distance and are most efficient close to the particle. Thus the hydrodynamic treatment is based on the boundary layer approximation, where the particle is replaced by a flat surface; cf. Fig. 4.

On a mesoscopic scale, van der Waals interactions are described in terms of the Hamaker constant H. This parameter is defined through the potential energy U per unit area A of two parallel bodies at a distance h [77],

$$\frac{U}{A} = -\frac{H}{6\pi h^2}.$$

Here we are interested in the forces exerted by a particle on the surrounding solvent and thus rewrite the potential energy density as

$$\frac{\varphi(z)}{V_s} = -\frac{H}{3\pi z^3}, \tag{62}$$

where V_s is the volume of a solvent molecule and z its distance from the particle surface.

The Hamaker constant H takes values of several 10^{-20} Joule, that is, about ten times the thermal energy, $H \sim 10 k_B T$. For non-polar materials, the Berthelot mixing rule

$$H = \sqrt{H_P H_S} \tag{63}$$

provides an approximate expression in terms of the Hamaker constants of the particle and the solvent material. It works less well for polar materials. For example, with the constants of polystyrene $H_P = 8\times10^{-20}$ J and of water $H_S = 5 \times 10^{-20}$ J one finds $\sqrt{H_P H_S} = 6.3 \times 10^{-20}$ J; the measured value $H = 1.3 \times 10^{-20}$ J is about five times smaller. In spite of this uncertainty we use the relation (63), simply because for most systems the interaction parameter H is not known.

The van der Waals potential energy φ diverges at $z = 0$, where the solvent molecules are in contact with the solute particle. This unphysical singularity is avoided by introducing a phenomenological cut-off d_0 related to the molecular structure; in a static situation this length may be viewed as the minimum distance of atomic dipoles on solute and solvent, and thus takes a value of one or two

Ångström. A modified picture arises in the present problem, where the shear force acts along the particle. The notion of a sheared fluid has no meaning at length scales below the size of the solvent molecules; this suggests to identify d_0 with the solvent molecular radius.

In an isotropic solvent, the dispersion forces on both sides of the particle cancel each other. A finite transport velocity arises from a spatial variation of the solvent concentration, $c(\mathbf{r}) = \bar{c} + \mathbf{r}\cdot\boldsymbol{\nabla} c$, with $\bar{c} = 1/V_s$. The resulting force on the solvent molecules reads as [122, 123]

$$\mathbf{f} = -c\boldsymbol{\nabla}\varphi. \tag{64}$$

Note that the gradient $\boldsymbol{\nabla}\varphi$ is perpendicular to the surface; hence there is no force along the particle, $f_x = 0$. Because of its weak variation over the size of the particle, $a|\boldsymbol{\nabla}\ln c| \ll 1$, the concentration may be taken constant in the normal force, $f_z = \bar{c}\partial_z\varphi$, and the perpendicular component of Stokes' equation (14a) is readily integrated,

$$P = P_0 - c\varphi. \tag{65}$$

Yet it is essential to retain the concentration gradient in the parallel component along the particle surface; evaluating Eq. (15) with $\partial_x P = -\varphi\partial_x c$, one finds the boundary velocity at a distance $B \gg d_0$,

$$v_B = -\frac{1}{\eta}\int_{d_0}^{B} dz z\frac{dP}{dx} = -\frac{H}{3\pi\eta d_0}\frac{\partial_x c}{\bar{c}}, \tag{66}$$

where $\partial_x c \propto \sin\theta$ depends on the polar angle. Dispersion forces being of short range, the parameter B corresponds to a few molecular layers from the particle surface.

The particle velocity takes the opposite sign and is directed towards higher density. In the present context, the non-unifiorm density is related to a thermal gradient. With the thermal expansivity

$$\beta = -\frac{1}{c}\frac{dc}{dT}$$

we find $\mathbf{u} = -D_T\boldsymbol{\nabla}T$ with the thermophoretic mobility

$$D_T = \frac{2\beta H}{9\pi\eta d_0}. \tag{67}$$

Except for water below 5 °C, liquids in general expand upon heating ($\beta > 0$); thus a temperature gradient drives particles to colder regions. With the parameter of common liquids one finds $D_T \sim 10\mu\mathrm{m}^2/\mathrm{Ks}$. Much higher values of $300\mu\mathrm{m}^2/\mathrm{Ks}$ were reported in an early experiment on polystyrene particles in water and hexane [124].

We stress that the macroscopic pressure is assumed to be constant throughout the sample. In agreement with the general theory of stationary non-equilibrium systems, the temperature gradient and the resulting density profile are not related to a pressure variation [1]. The excess pressure (65) arises from the solute-solvent forces and thus vanishes rapidly beyond a few nanometers from the solute surface.

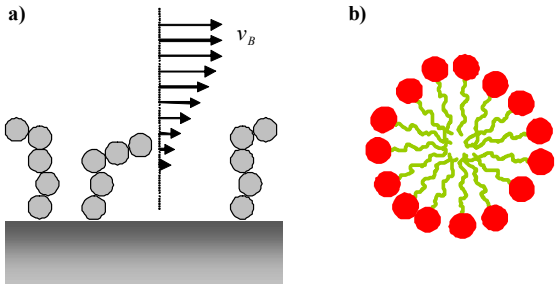

FIG. 16: a) Schematic view of a charged polystyrene particle. Because of the ionic molecular groups grafted on its surface, the "plane of shear", where the lateral velocity vanishes, is at a distance d_0 that corresponds to the size of the surfactant. b) Micelle of ionic surfactants; their electrostic interaction keep the surface smooth, and the cut-off distance d_0 is given by the size of a water molecule.

C. Dispersion forces in aqueous solution

For charged colloids in aqueous solutions both electric-double layer and dispersion forces contribute to the thermophoretic mobility. With a surface potential $\zeta \sim 50$ mV and the viscosity $\eta \sim 10^{-3}$ Pa.s of water, the electric part in Eq. (38) takes the value

$$\frac{\varepsilon\zeta^2}{3\eta} \sim 2\mu\mathrm{m}^2/\mathrm{Ks}.$$

Evaluation of the term driven by dispersion forces is less simple, since the cut-off parameter d_0 appearing in Eq. (67) may take rather different values, depending on the solute surface properties. Moreover, the Hamaker interaction parameter H of organic materials in aqueous solution is not well known. Finally, the thermal expansion coefficient β varies strongly with temperature. It vanishes at 4° C because of the density anomaly of water, then increases steadily up to the boiling point: $\beta = 0$ (4° C); $\beta = 0.2\times10^3$ K^{-1} (20° C); $\beta = 0.5\times10^3$ K^{-1} (50° C). Therefore the mobility (67) vanishes close to the freezing point, but may take significant values above room temperature.

As a first example, consider a suspension of charged polystyrene particles. The surface charge density σ stems from ionic molecular groups grafted at the particle surface. As illustrated by Fig. 16a, these groups shift the "plane of shear" by a distance d_0 into the solvent. Hamaker constants for the interaction of polar and non-polar materials are rather small. Evaluating (67) with $d_0 \sim 1$ nm, $H \sim 2\times10^{-20}$ J, and the thermal expansivity at 20° C, we find $D_T \sim 0.3\mu\mathrm{m}^2/\mathrm{Ks}$. This is significantly smaller than the electric contribution, suggesting that van der Waals forces are of little relevance for thermophoresis of polystyrene particles in water. This statement is confirmed by the measured variation of D_T with the electrolyte strength.

As a counterexample, we sketch in Fig. 16b a SDS micelle. The headgroup interactions keep the surface smooth, such that the cut-off parameter corresponds to the size of water molecule, $d_0 \sim 0.2$ nm. Because the polar headgroups interact more efficiently with the surrounding water, one may assume a larger Hamaker constant, $H \sim 4 \times 10^{-20}$ J. With these parameters one has $D_T \sim 2\mu\text{m}^2/\text{Ks}$, which is comparable to the double-layer contribution.

These remarks suggest that the van der Waals interaction and the electric-double layer forces may contribute to the thermophoretic mobility. The dependencies on salinity and temperature give clues about which term prevails in a given system, and how to separate their respective contributions. For example, Piazza and Guarino found that D_T of dilute SDS micelles increases almost linearly with the inverse salinity. In view of $D_T \propto \zeta^2$ and the variation of the surface potential with salinity ($\zeta^2 \propto 1/n_0$ for weak coupling), this observation indicates that, at least at room temperature, the micellar motion is driven by double-layer forces [4].

Regarding the temperature dependence, Piazza and coworkers [32, 33] and Brenner [47] have pointed out that D_T of SDS micelles, proteins, and DNA, is strongly correlated with the thermal expansion coefficient β of water; in view of Eq. (67) this would indicate dispersion forces to be relevant. On the other hand, the fit of Fig. 11 suggests that double-layer forces show a similar increase with temperature, and Eq. (42) is supported by the established proportionality between the thermal expansivity and the salt Soret coefficient [28].

D. The effect of coating

In a study on the Soret motion of octadecyl coated silica particles in toluene, Wiegand and co-workers found an inverse Soret effect ($D_T < 0$) at room temperature; upon heating the thermophoretic mobility increases linearly with T, changes sign at about 40° C, and becomes positive at higher temperature [7]. These findings are surprising for two reasons: First, for an uncharged systems one would expect $D_T > 0$: According to Eq. (67) the van der Waals interaction with the solvent forces drive the particle towards the cold. Second, since its parameters hardly depend on temperature, the mobility D_T should be roughly constant with respect to T.

The D_T values measured for dilute suspensions vary in the range $\pm 0.4\ \mu\text{m}^2/\text{sK}$[7]; this is by one order of magnitude smaller than what is usually found for organic systems; see, for example, the numbers for polystyrene in Fig. 19 below. This low thermophoretic mobility can be explained through the surface roughness due to coating and the high thermal conductivity of silica. According to the discussion Fig. 16a, the octodecyl groups grafted on the silica beads shift the plane of shear by a distance $d_0 \sim 1$ nm into the solvent and thus reduce the thermoosmotic flow. On the other hand, the heat conductivity of toluene $\kappa_S = 0.13$ W/mK is by almost one order of magnitude smaller than that of silica, $\kappa_P = 1.1$ W/mK. According to (24) this ratio reduces the temperature gradient at the particle surface by about 70%. With the properties of toluene and $H \sim 10^{-20}$ J we obtain

$$D_T^0 = \frac{3\kappa_S}{2\kappa_S + \kappa_P} \frac{2\beta H}{9\pi\eta d_0} \sim 0.3\mu\text{m}^2/\text{Ks},$$

in qualitative agreement with the measured values.

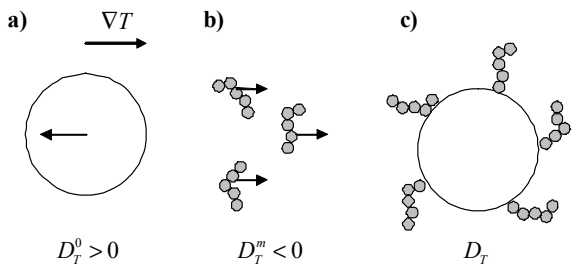

FIG. 17: Schematic view of thermophoresis of a coated particle. a) Dispersion forces drive the particle to higher solvent density and thus lower temperature. b) Small molecular solvents, such as octodecane in toluene, show an inverse Soret effect and rather diffuse to the warm. c) The combination of both mechanisms may drive the coated particle in either direction.

As an important clue to the puzzling sign of D_T of coated silica beads, Wiegand and co-workers observed that octodecane molecules in toluene show a negative Soret effect, $D_T^m = -5\mu\text{m}^2/\text{sK}$. This does not come as a surprise; as discussed in detail in Sect. V, because of their random wriggling through the sample, small molecules are subject to an additional negative Soret contribution, which may lead to $D_T^m < 0$.

As illustrated in Fig. 17, a silica bead is subject to two opposite thermal driving mechanisms,

$$D_T = D_T^0 + \chi D_T^m,$$

where the first one accounts for the dispersion forces between the bead and the solvent, and the second one for the negative Soret effect of the molecular groups grafted on its surface. From this picture one expects long and flexible coating molecules to be more efficient. The factor χ accounts for the reduced mobility of the octodecyl groups; its temperature dependence could result in the change of sign reported in Ref. [7]. The detailed physical mechanism remains to be elucidated.

IV. POLYMER THERMOPHORESIS

A. Hydrodynamic interactions

When averaging over the configurations of a polymer in three-dimensional space, one finds that the molecule

occupies a volume $\sim R^3$; the characteristic length R is given by the gyration radius which varies with the number N of beads as

$$R = \ell N^\nu.$$

For a flexible and ideal polymer, $\ell = 2a$ is the size of a building block, and the exponent ν takes the value $\frac{1}{2}$; for real chains in a good solvent, one has $\nu \approx \frac{3}{5}$ [125].

If the polymer is subject to an applied force such as gravity, or simply the Langevin force due to the thermal fluctuations of the solvent, the resulting velocity depends strongly on N and thus on the molecular weight M_w. Each bead induces in the surrounding fluid a velocity $\mathbf{v}_F(\mathbf{r}) \sim 1/r$ that is proportional to the inverse distance. When considering the velocity of a given bead n, one has to sum over the flow due to all parts of the molecular chain; evaluating the response to the Langevin force and the corresponding mean-square displacement, one finds the Einstein coefficient [125]

$$D = \frac{k_B T}{6\pi\eta R_h}, \tag{68}$$

where the hydrodynamic radius R_h is closely related to R; in the following we use $R_h \approx 0.7R$ [126]. With respect to that of a single bead, $k_B T/6\pi\eta a$, hydrodynamic interactions reduce the diffusion coefficient by a factor a/R_h. Thus a polymer of 10^5 repeat units diffuses about thousand times more slowly than a monomer. As illustrated in Fig. 18a, the molecular chain drags a volume $\frac{4}{3}\pi R_h^3$; note that the figure shows the fluid velocity field in the frame attached to the molecule.

A rather different situation occurs for the motion driven by thermoosmosis, where the velocity of high polymers in dilute solution is independent of the molecular weight M_w [34]. In Fig. 19 we plot values measured by Giddings and co-workers for polystyrene in different solvents, in the range from $M_w = 20000$ to 160000 [35]; despite their scatter these data give clear evidence that D_T is constant with respect to M_w. This has been confirmed for other polymers and extended to an even larger range of M_w [9, 37, 127–129].

Brochard and de Gennes showed that this property is related to the fact that thermophoresis is insensitive to hydrodynamic interactions within the polymer chain. In dilute solution, the intermolecular distance is much larger than the gyration radius, and it is sufficient to consider a single molecular chain of N beads at positions $\mathbf{r}_n$. According to Eq. (67), the non-uniform solvent concentration imposes on each molecular unit a transport velocity $\mathbf{u}$. In addition, it experiences the velocity field induced by the motion of the other beads m. As a consequence, at any instance the velocity of a given mer n is obtained by adding to the single-bead velocity the flow induced by the neighbors,

$$\mathbf{U}_n = \mathbf{u} + \sum_{m\neq n} \mathbf{v}(\mathbf{r}_n - \mathbf{r}_m), \tag{69}$$

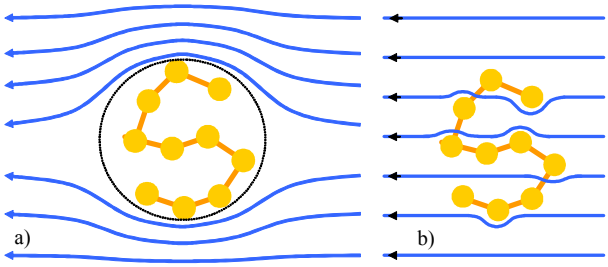

FIG. 18: Fluid velocity field $\mathbf{v}(\mathbf{r})$ in the frame attached to a soluted polymer. a) Body forces such as gravity; because of hydrodynamic interactions, the polymer retains a fluid volume $\sim R^3$. b) In the case of osmosis-driven motion, there are no hydrodynamic interactions, and the fluid passing through the polymer is hardly perturbed. (Reprinted from Ref. [72].)

where $\mathbf{v}(\mathbf{r})$ is given in Eq. (17).

The velocity $\mathbf{v}(\mathbf{r})$ and the resulting shear are so weak that they do not affect the statistical properties of the polymer; in other words, the external field ∇T is treated in linear response approximation. In particular there is no orientational order of nearby polymer beads with respect to the thermal gradient. When integrating over the spatial orientation of the distance vector $\mathbf{r}_n - \mathbf{r}_m$, i.e., the polar angle θ in (17), one finds that the mean drag field vanishes,

$$\langle \mathbf{v}(\mathbf{r}_n - \mathbf{r}_m)\rangle = 0. \tag{70}$$

Each mer drifts with mean velocity $\langle \mathbf{U}_n\rangle = \mathbf{u}$, and so does the polymer as a whole, independently of its length and branching structure. In the frame attached to the molecule this means that the fluid flows through the polymer coil without significant perturbation, as illustrated in Fig. 18b.

As a consequence, the thermophoretic mobility of a polymer chain does not depend on the number of beads and is given by Eq. (67),

$$D_T = \frac{2\beta H}{9\pi\eta d_0}. \tag{71}$$

The numerical prefactor of this expression has been obtained from hydrodynamics, that is for a structureless solvent, and for solutes much larger than the range of their interactions. One should keep in mind that, all molecular units being of comparable size, these assumptions are not really justified for a polymer in an organic solvent.

B. Soret coefficient

The results of the preceding sections, in particular the constant mobility D_T, rely on the fact that polymer thermophoresis is insensitive to hydrodynamic interactions. On the other hand, diffusion becomes slow for

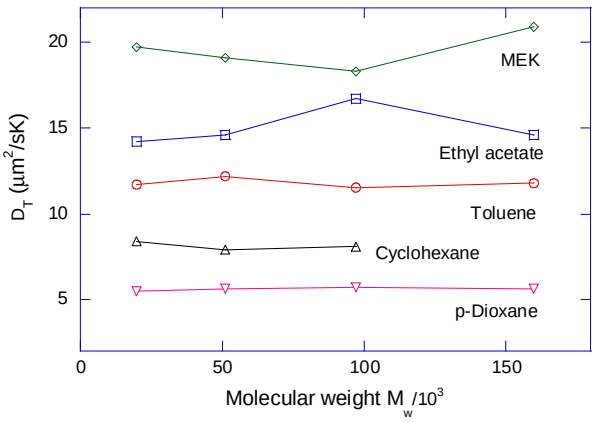

FIG. 19: Molecular weight dependence of the thermophoretic mobility of polystyrene in different solvents at about 30° C. The data are from Ref. [35]; the lines are a guide to the eye. The mass of styrene -(C_8H_8)- corresponds to 104 atomic units or 104 g/Mol. Thus the investigated polymers range from 200 to about 1600 repeat units.

long chains; because of the large fluid volume dragged by a polymer, its diffusion coefficient (72) varies with the inverse hydrodynamic radius. As a consequence, the Soret coefficient $S_T = D_T/D$ is proportional to R_h and increases with the molecular weight as N^ν. Multiplying with temperature we obtain the dimensionless quantity

$$TS_T = \frac{4R_h}{3d_0}\frac{\beta H}{k_B}, \tag{72}$$

which corresponds to Giddings' thermal diffusion factor α [35]. With known values of the thermal expansivity and the Hamaker constant one has $\beta H/k_B \approx 2$; the variation of the hydrodynamic radius with N results in $TS_T \propto N^\nu$. This power law compares well with measured data for polystyrene [35], and has been confirmed for many systems.

At the largest molecular weight $M_w = 16 \times 10^4$ of Ref. [35], the Soret coefficient attains the value $S_T \approx 0.3\ \mathrm{K}^{-1}$. A temperature variation ΔT leads to a change in polymer concentration by the factor $e^{-\Delta T S_T}$. Heating one side of the sample by five percent in absolute temperature, or $\Delta T = 15$ K, enhances the polymer concentration in the colder region by a factor of 90, that is almost two orders of magnitude.

C. Solvent properties

The data of Fig. 19 and more recent experiments show that the absolute value of D_T varies strongly from one solvent to the other. In Table III we compare the measured mobility D_T, the solvent parameters β and η, and the effective Hamaker constant $H = \sqrt{H_p H_s}$, and determine the cut-off length d_0. As discussed in detail by previous authors [10, 122, 130], the numbers of the second and third columns confirms the relation $D_T \propto 1/\eta$, and give evidence that the dispersion of the mobility data stems to large extent from the solvent viscosity.

In the last column we determine the cut-off distance d_0 according to (71). In itself, this quantity is of limited physical meaning; it has been introduced in order to regularize the divergence that arises from the continuous-body approximation (62) for the van der Waals interaction. In the present context it is of some interest as a signature for the validity of the continuous-solvent model: Eq. (71) has been obtained by treating the solute as a macroscopic body and by neglecting the solvent molecular structure. These assumptions are questionable for polymer beads that are of the same size as the solvent molecules. Regarding polystyrene, the values in the last column of Table III range from 0.6 to 1 nm; these numbers roughly correspond to the size of a solvent molecule calculated in Ref. [131]. This agreement rather supports the hydrodynamic approach to the transport coefficient D_T: The notion of a velocity field ceases to be meaningful at distances shorter than the molecular size.

Analyzing data for five different polymers, Hartung and Köhler found a significant correlation between the mass of a single bead of the polymer chain and the coefficient D_T [130]. The biggest values of D_T occur for the polymers with the largest mass, poly-α-methylstyrene (PαMS, 118 g/Mol), polystyrene (PS, 104), and polymethylmethacrylate (PMMA, 100). On the other hand, polyisoprene (PI, 68) and poly-dimethylsiloxane (PDMS, 74), are built of lighter repeat units and show mobilities that are by a factor of 2 or 3 smaller. This ratio holds true for several solvents.

TABLE III: Thermophoretic mobility D_T of polystyrene at 22° C in different solvents of viscosity η and thermal expansivity β ; the data are from [130] with the Hamaker constant $H_p = 8.1 \times 10^{-20}$ J. The last line accounts for polyethylen glycol in water at 25° C, with $H_p = 6 \times 10^{-20}$ J and $D_T = 5.9\mu\mathrm{m}^2/\mathrm{Ks}$ from Fig. 25. We use the Berthelot mixing rule $H = \sqrt{H_p H_s}$. The cutoff length is calculated according to Eq. (67).

Polymer/solvent	m_S amu	D_T $\frac{\mu\mathrm{m}^2}{\mathrm{sK}}$	$10^3\eta$ Pa.s	$10^3\beta$ K^{-1}	H_s 10^{-20} J	d_0 Å
PS/MEK	72	18	0.39	1.32	4.6	6.1
PS/ethyl acetate	88	13	0.44	1.38	4.2	7.2
PS/toluene	92	11	0.57	1.07		
PS/THF	72	10	0.48	1.29	5.7	10.8
PS/benzene	78	8	0.63	1.23	5.0	8.6
PS/cyclohexane	84	7	0.95	1.23	5.2	6.8
PS/cyclooctane	112	3	2.42	0.98		
PEG/water	18	6	0.95	0.25	5.0	1.3

D. Temperature dependence

The transport coefficient D_T varies with solvent viscosity and thermal expansivity, and the Soret coefficient with the molecular weight. These dependencies are well understood, as illustrated by the good agreement of the theoretical expressions with various experimental findings [8, 11, 37, 127, 129, 132]. The situation is less clear regarding their variation with temperature. In view of Eq. (71) we note that both the Hamaker parameter and the thermal expansivity β are constant with respect to T. By contrast, the viscosity changes significantly, according to

$$\eta = ATe^{B/T}, \tag{73}$$

where T is the absolute temperature. The resulting Arrhenius law for the Einstein coefficient $D \propto e^{-B/T}$ is confirmed by experiment [35], where the activation energy B may be viewed as hindering potential of elementary molecular jumps. Assuming the other parameters in Eq. (17) to be constant, one would expect a similar behavior for the thermophoretic mobility $D_T \propto (1/T)e^{-B/T}$. On the other hand, the viscosity factors cancel in the Soret coefficient, and the reduced quantity TS_T should be independent of temperature.

Fig. 20 shows mobility and Soret data for polystyrene in ethylbenzene between 0° and 75 °C [35]. From 0 to 40 °C the coefficient D_T increases by about 25 percent and saturates at higher temperatures. The solid curve is calculated fro Eq. (17), with the constants $H/d_0 = 2{\times}10^{-10}$ J/m and $\beta = 10^{-3}$ K^{-1}; for the solvent viscosity we take $A = 1.9 \times 10^{-8}$ Pa·s/K and $B = 1400$ K. Although the temperature dependence of the viscosity accounts qualitatively for the increase of D_T, there are significant discrepancies: The slope of the theoretical curve is larger than that of the experimental data, and at higher temperature it does not account for the observed saturation [35]. This indicates that the strong variation of $1/\eta$ is attenuated by another factor which decreases with rising T; as a consequence D_T increases more weakly than D. This is confirmed by the Soret data shown in the lower panel, where the additional factor in D_T results in a moderate decrease of the coefficient TS_T with rising temperature. The data of Fig. 20 at 0° and 70 °C differ by about 30%, independently of the molecular weight. Though this observation has been made more than 30 years ago, there is still no satisfactory explanation.

Enge and Köhler reported a similar discrepancy for mixtures of poly-ethylmethyl-siloxane (PEMS) and polydimethyl-siloxane (PDMS) in the temperature range between 280 and 370 K [133]. Both the Einstein coefficient D and the thermophoretic mobility D_T show Arrhenius behavior, albeit with different activation energies. As a consequence, augmenting the temperature from 280 to 370 K reduces the Soret coefficient S_T by a factor 2. This additional temperature dependent factor is the same for different PEMS/PDMS mixtures; it does not change with the molecular weight.

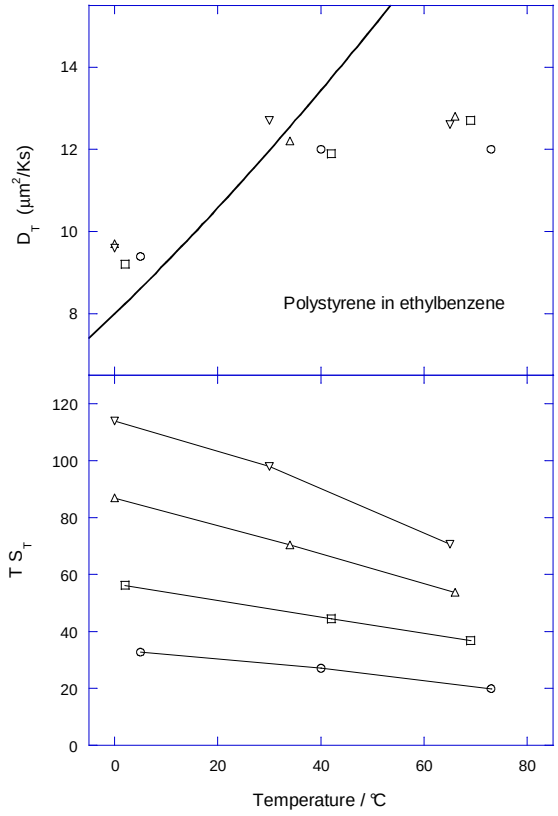

FIG. 20: Upper panel: Thermal diffusion coefficient D_T of polystryrene in ethylbenzene, as a function of temperature. The data are taken from Ref. [35] for molecular weights 19800 (O), 51000 (□), 97200 (△), 160000 (▽). The curve is given by Eq. (17) with a temperature dependent viscosity as discussed in the main text. (Reprinted with permission from Ref. [98]. Copyright 2009 American Chemical Society.) Lower panel: Reduced Soret coefficient for the same parameters. The lines are a guide to the eye.

E. Semidilute solutions

In dilute solutions the distance between neighbor chains is much larger than the gyration radius. Then the polymer coils don't overlap, interactions are irrelevant, and the thermophoretic mobility is independent of the molecular weight. Experimental studies at higher polymer concentration show that the mobility decreases in dense solutions. Here we discuss a few aspects of the semidilute case where interaction effects set in and modify the single-chain picture.

In the simplest approach, hydrodynamic coupling of nearby molecules is accounted for by a concentration dependent viscosity. Einstein's formula $\eta = \eta_0(1 + \frac{5}{2}\phi)$ describes viscous thickening due to the volume fraction ϕ of colloidal particles. Polymers give rise to a similar behavior albeit with an effective volume $\frac{4}{3}\pi R_h^3$ per mole-

cule, where $R_h = 2aN^\nu$ is the hydrodynamic radius [134]. Thus one finds for the viscosity as a function of the polymer content ϕ and the number of beads N per chain,

$$\eta = \eta_0 \left(1 + CN^{3\nu-1}\phi\right). \tag{74}$$

The numerical constant C depends on the persistence length and the detailed molecular structure. As an example for the resulting decrease of the thermophoretic mobility, Fig. 25 shows data of Chan et al. for polyethylene glycol in aqueous solution [8]. In this experiment the chain length N is varied at a constant ethyleneoxide concentration of 9 g/l, The decrease of D_T for long chains, $N > 20$, is well described by Eq. (74) with $C = 0.9$ and $\nu = \frac{1}{2}$.

A more significant molecular-weight dependence of D_T has been observed for several polyelectrolytes. For sodium polystyrene sulfonate (NaPSS) in 100 mM/l NaCl solution, Iacopini et al. [33] found a reduction by about one third upon increasing the chain length N from 74 to 360 at constant polymer content of 2 g/l. This observation cannot be explained by Eq. (74): The same variation with N occurs for the Soret coefficient $S_T = D_T/D$, which does, however, not depend on viscosity. Thus the effect of the PSS chain length is not related to viscous thickening, indicating the existence of another mechanism that reduces the thermophoretic mobility of long polyelectrolytes. This conclusion is confirmed by Duhr and Braun's data on DNA [6]: At a constant base pair concentration of 50 μM/l, an increase of their number per molecule from $N = 50$ to 48500, reduces D_T by a factor of five. The strongest variation occurs for rather short chains, $N < 10^3$, where the quantity $N^{3\nu-1}\phi$ is smaller than 10^{-3} and where the viscosity is not affected by the presence of the polymer.

V. MOLECULAR-WEIGHT DEPENDENCE

So far we have evaluated the thermophoretic mobility by inserting the interfacial forces in Stokes' equation. Treating the solute as a macroscopic body, we have neglected its Brownian motion when calculating D_T. Moreover, this hydrodynamic approach takes the solvent as a continuous medium and does not account for its molecular diffusivity [47, 48]. These assumptions are justified for big particles and high polymers, as long as their size and gyration radius are much larger than the length scales set by the interaction and by the solvent molecular structure.

Clearly, this is not the case for binary mixtures of small molecules, where solute and solvent size, and the range of the dispersion forces are of the order of one nanometer. As a consequence, beyond the hydrodynamic treatment, molecular diffusion in a thermal gradient has to be taken into account. In analogy to the Rayleigh piston shown in Fig. 3b, both solute and solvent molecules undergo Brownian motion and thus visit regions of lower and higher temperatures. Because of the gain in chemical potential, they are slightly more eager to stay at the cold side. It turns out that the competing forces depend in a subtle way on the ratio of solute and solvent molar mass, and on the mutual interaction. Thus it is not surprising that in dilute molecular mixtures the thermophoretic mobility may take both signs.

A. Non-equilibrium thermodynamics

The stationary state of a non-equilibrium system corresponds to a minimum of the entropy production rate σ per unit volume [1], which is a bilinear form of generalized fluxes and forces, that is, the time derivatives of the dynamics variables and the corresponding driving fields. Onsager's phenomenological equations relate these fluxes and forces; the steady state of a closed system without chemical reactions is described by zero currents.

As a simple example consider the electric current density j flowing in a metallic wire upon application of an electric field E. The frictional forces on the charge carriers dissipate energy; the heat produced in a volume V per unit time reads $\dot{Q} = jEV$, and the entropy $\dot{S} = \dot{Q}/T$. Thus we find the entropy production rate per unit volume

$$\sigma = \frac{jE}{T}. \tag{75}$$

Non-equilibrium thermodynamics deals with linear force-current relations like Ohm's law $j \propto E$ but does not provide a framework for calculating the transport coefficients. In the present example, the electric conductivity j/E is obtained from kinetic theory for electrons in a metal.

Generalizing this scheme to a binary mixture of molecular species $i = p, s$ with a non-uniform temperature, one obtains the rate of entropy production as a bilinear form of generalized fluxes and forces [1],

$$\sigma = \mathbf{J}_Q \cdot \boldsymbol{\nabla}\frac{1}{T} + \frac{1}{T}\sum_i \mathbf{J}_i \cdot \mathbf{K}_i. \tag{76}$$

The heat flow $\mathbf{J}_Q$ is related to $\boldsymbol{\nabla}(1/T)$, and the particle currents $\mathbf{J}_i$ to the thermodynamic forces that comprise the gradients of temperature and the chemical potentials μ,

$$\mathbf{K}_i = -T\boldsymbol{\nabla}\frac{\mu_i}{T}. \tag{77}$$

In the steady state of a multicomponent system, one of the concentrations can be eliminated. For a binary system with volume fractions $\phi_1 = \phi = 1 - \phi_2$, Onsager's "phenomenological equations" thus reduce to the heat and mass currents

$$\mathbf{J}_Q = -\kappa\boldsymbol{\nabla}T - D_F\boldsymbol{\nabla}\phi, \tag{78a}$$

$$\mathbf{J}_1 = -D\boldsymbol{\nabla}\phi - \phi(1-\phi)D_T\boldsymbol{\nabla}T. \tag{78b}$$

The diagonal terms account for heat conductivity with coefficient κ and for particle diffusion with the Einstein

coefficient D. The Dufour coefficient D_F describes heat flow due to a non-uniform solute concentration; whereas the thermophoretic mobility D_T accounts for motion driven by the thermal gradient. In linear-response approximation, the coefficient are related to the equilibrium current-current correlation functions [135].

Onsager's theory establishes linear relations between forces and currents, and symmetry properties of off-diagonal transport coefficients such D_F and D_T; it does not provide an explicit scheme for calculating them. In the hydrodynamic approach which the preceding sections rely on, this is achieved by treating the colloidal particle as a macroscopic object in a homogeneous fluid. The interfacial forces maintain the motion of the solute; the resulting flow in the viscous fluid produces entropy at a rate [1]

$$\sigma = -\frac{\mathbf{\Pi} : \mathbf{\Sigma}}{T}, \tag{79}$$

which is the contraction of the velocity derivatives $\Sigma_{\alpha\beta} = \partial_\beta v_\alpha + \partial_\alpha v_\beta$ and the viscous pressure $\Pi_{\alpha\beta}$. Just as Ohm's law relates the electrical current to the applied field, the viscous pressure is determined by the derivative of the velocity field through $\mathbf{\Pi} = -\eta\mathbf{\Sigma}$, with the viscosity η as "phenomenological coefficient". The equation of motion of a fluid volume element

$$\rho\partial_t \mathbf{v} = \mathbf{f} - \boldsymbol{\nabla} P - \boldsymbol{\nabla}\cdot\mathbf{\Pi}$$

comprises, beyond the force $\mathbf{f}$ exerted by the particle surface, the hydrostatic and viscous pressure components. In the steady state $\partial_t \mathbf{v} = 0$; inserting $\mathbf{\Pi} = -\eta\mathbf{\Sigma}$ and noting $\boldsymbol{\nabla}\cdot\mathbf{v} = 0$, one readily recovers Stokes' equation (14a).

In this hydrodynamic picture the solvent is treated as a continuous medium; it neglects both the solvent molecular diffusivity [47] and fluctuations [48]. In the limit of very small particles or short solute molecules, however, the molecular structure of the solvent becomes important. Then the picture of a macroscopic solute in a uniform medium breaks down, and one has to consider diffusion of each species of a molecular mixture.

B. Thermodiffusion

The thermodiffusion solute flow $\mathbf{J}$ is determined by the generalized forces $\mathbf{K}_i$ that are given by chemical potential and temperature gradients. As a simple model we consider a binary mixture of beads of equal size but different interaction potential. The chemical potential μ_i comprises the translational entropy and the interaction free energy $-\epsilon_i$. The latter arises from the van der Waals potential of nearby molecules, and is closely related to the Hamaker constant. In a denser system, there are more nearby neighbor molecules, and the van der Waals binding energy increases accordingly. In the simplest picture, the gradient of the free-energy parameter

$$\boldsymbol{\nabla}\epsilon_i = -\epsilon_i\beta\boldsymbol{\nabla}T \tag{80}$$

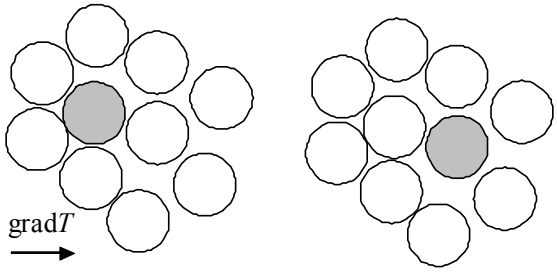

FIG. 21: Thermal diffusion of a single bead. The solute (in grey) has a tendency to diffuse towards higher solvent density or lower temperature. The same is true for the solvent molecules; the two terms of Eq. (81) account for this competition. The solute moves to the cold if its van der Waals energy exceeds that of a solvent molecule $\epsilon_p > \epsilon_s$; otherwise it is pushed towards the warm.

is determined by the thermal expansivity β.

The generalized forces are readily obtained by inserting μ_i in (77). The actual problem consists in determining the corresponding mobilities. The following discussion relies on the assumption that all mobilities are given by the friction coefficient $6\pi\eta a$ due to Stokes drag of a sphere of radius a. The gradient of the volume fraction gives rise to the Fick diffusion current $-D\boldsymbol{\nabla}\phi$; here we are interested in the additional terms due to the temperature gradient. From the condition of zero overall flow $\mathbf{J}_1 + \mathbf{J}_2 = 0$, one derives the transport coefficient defined in (78b),

$$D_T = \frac{\epsilon_1 - \epsilon_2}{6\pi\eta a}\left(\beta + \frac{1}{T}\right). \tag{81}$$

The terms depending on the thermal expansivity β arise from the non-uniform dispersion forces that attract each molecule towards higher mass density and thus towards lower temperature. The remaining ones, proportional to $1/T$, account for the entropy of a given molecule wriggling in the cage formed by its neighbors; in a non-uniform system this gives rise to a net force. Because of the assumptions on the mobility factor, Eqs. (80) and (81) should be considered as a qualitative expression for the two contributions in the thermal forces $\mathbf{K}_i$.

The occurrence of the difference of the free energies ϵ_1 and ϵ_2 has a simple physical meaning: As illustrated in Fig. 21, the migrating solute bead "1" requires a solvent molecule to move in the opposite direction; the net velocity is determined by the difference of their respective force and thus proportional to $\epsilon_1 - \epsilon_2$. Comparing with the transport coefficient (67) derived for a particle much larger than the solvent molecules, and putting $\epsilon_1 \sim H$ and $a \sim d_0$, one recovers the term proportional to $\beta\epsilon_1$ in (81). This implies that the remainder vanishes in the limit of large solute particles.

Through the van der Waals interactions, D_T depends on the fraction ϕ of solute molecules. In a mean-field approach, the single-molecules energies may be written

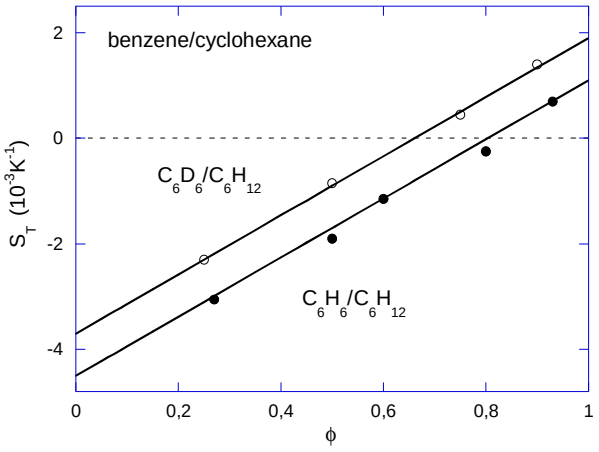

FIG. 22: Soret coefficient of benzene in cyclohexane as a function of relative benzene content ϕ.In the dilute limit benzene diffuses to the warm ($S_T < 0$); the Soret coefficient increases linearly with ϕ and changes sign at $\phi \approx 0.7$. Full and open symbols indicate protonated and deuterated benzene, respectively. The data are from Debuschewitz and Köhler [38].

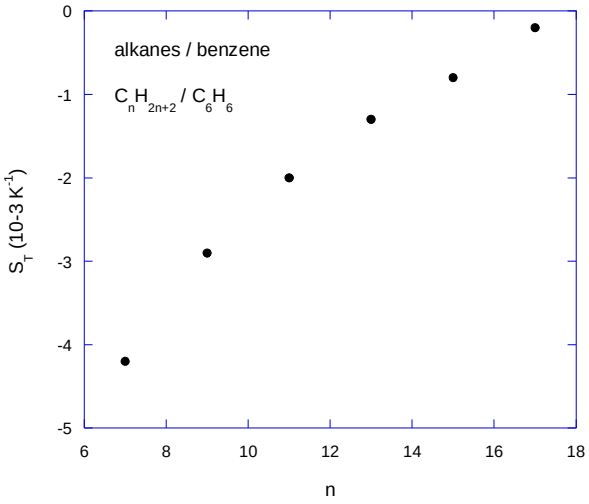

FIG. 23: Soret coefficient of normal alkanes in benzene at equal mol fractions. Starting from heptane, short alkanes show a strong negative Soret effect; their S_T increases with increasing number of ethylen units and would become positive for $n > 18$. The data are from Polyakov and Wiegand [137].

as $\epsilon_1 = \phi\epsilon_{11} + (1-\phi)\epsilon_{12}$ and $\epsilon_2 = \phi\epsilon_{12} + (1-\phi)\epsilon_{22}$, where the coupling parameters ϵ_{ik} are closely related to the Hamaker constants. Defining $\epsilon_0 = \epsilon_{12} - \epsilon_{22}$ and $\epsilon = \epsilon_{11} + \epsilon_{22} - 2\epsilon_{12}$ one finds

$$D_T = \frac{\epsilon_0 + \phi\epsilon}{6\pi\eta a}\left(\frac{1}{T} + \beta\right). \tag{82}$$

This simple model with the chemical potentials μ_i, equal molecular radii, and Stokes drag, accounts for a number of experimental observations. Eq. (81) may be positive or negative, depending on the difference of the molecular energies; indeed, both signs of D_T occur in molecular mixtures [38, 136–138]. Moreover, for alcohol in water and several binary mixtures of organic molecules, an almost linear variation of D_T with ϕ has been observed, in accord with Eq. (82). In Fig. 22 we plot Soret data of Debuschewitz and Köhler for normal and deuterated benzene in cyclohexane [38]. In the dilute case benzene shows an inverse Soret effect. The coefficient S_T increases linearly with the relative benzene content ϕ and changes sign at about 80%, implying $0 < -\epsilon_0 < \epsilon$.

C. Mass and volume effects

Experiments on binary molecular mixtures indicate that the molecular mass and volume are essential parameters. As a rule of thumb, heavy and large molecules diffuse to the cold, whereas small and light molecules rather show the opposite tendency [38, 138]. This observation has been related to the fact that light particles carry mainly kinetic energy, which is larger at high T, whereas the energy flow due to the larger component involves rather molecular interactions which prevail at the cold side [139]; this argument agrees with Chapman's theoretical result (8) for thermal diffusion in gases.

As an illustration of the mass effect in liquids, Fig. 22 shows that deuterated benzene ($m = 84$ amu) has a more positive Soret coefficient than the protonated isomer ($m = 78$ amu). Since their size and shape are identical, the excess contribution $\Delta S_T \approx 0.8 \times 10^{-3}$ K^{-1} of deuterated benzene is related to the mass difference. As expected the heavier isotope has a tendency to move towards lower temperatures. Debuschewitz and Köhler have investigated a variety of fully or partially deuterated molecular mixtures [38]; their analysis gives evidence that the Soret coefficient is the sum of independent mass and chemical contributions. This mass effect is confirmed by molecular dynamics simulations of Reith and Müller-Plathe, for spherical beads of equal size but different mass [140].

The volume difference is a relevant parameter for binary mixtures of molecules of different size but roughly constant mass density. As an example for the size dependence, Fig. 23 shows data by Wiegand and co-workers for mixtures of normal alkanes C_nH_{2n+2} and benzene [137]; the strongest inverse Soret effect occurs for the shortest molecule investigated ($n = 7$). The coefficient increases with the number of ethylene units, suggesting a change sign beyond octodecane ($n = 18$). The many data on binary mixtures of normal alkanes of different length confirm the rule that the larger molecules migrates to the cold [141].

Volume effects have been widely discussed in the liter-

ature, and there are various attempts to generalize the transport coefficient (81) by introducing weight factors depending on the molecular volume or mass ratio. In the heat-of-transport approach [142–145], the Soret coefficient is obtained from the Gibbs-Duhem equation, resulting in the volume dependence

$$S_T = \frac{Q_1 V_2 - Q_2 V_1}{\bar{V} k_B T^2}, \tag{83}$$

with $\bar{V} = \phi V_1 + (1-\phi)V_2$. Similar expressions have been proposed with the molecular masses instead of the volumes. Artola and Rousseau have discussed several of these models and compared with their molecular dynamics simulations [146]. The heat-of-transport parameters Q_i are mostly related to the molecular energies or enthalpies. For $V_1 = V_2$ and noting $S_T = D_T/D$, one readily establishes the link to Eq. (81).

It turns out instructive to discuss (83) for a dilute suspension of large molecules. With $\phi \to 0$ the volume dependence simplifies to $S_T \propto Q_1 - (V_1/V_2)Q_2$; thus the Soret coefficient is proportional to the solute volume and an extensive quantity for $V_1 \gg V_2$. Since the diffusion coefficient varies with the inverse solute size, this volume dependence implies that the thermophoretic mobility $D_T = S_T D \propto V_1^{2/3}$ varies with the square of the particle radius. Yet this dependence contradicts the well-known fact that electrophoretic and thermophoretic velocities of large particles are independent of the size, as discussed below Eq. (50). In agreement with this statement, recent MD simulations of Galliéro and Volz find that, for the aspect ratio a_1/a_2 ranging from 2 to 12, the coefficient D_T is independent of the solute size whereas D is proportional to $1/a$ [147]. These findings shed some doubt on the physical meaning of Eq. (83).

D. Thermoosmosis versus thermal diffusion

The above approach to thermal diffusion for small solutes is complementary to thermoosmotic driving studied in Sects. II and IV. Here we discuss the cross-over between these pictures, that is, we address the question how polymer thermophoresis depends on the number of beads in a single chain N, or the molecular weight M_w.

Studies on various polymers show that in the range $M_w > 20$ kg/M the thermophoretic mobility is independent of the molecular weight. According to recent measurements by Köhler and co-workers, this rule ceases to be valid for shorter chains [9, 10], as illustrated in Fig. 24 by data for polystyrene in several solvents. With the mass $m = 104$ g/M of a styrene unit, the plotted range from 0.1 to 10^3 kg/M corresponds to 1...10^4 repeat units. For long chains ($M_w > 10$ kg/M or $N > 100$) the mobility D_T is constant indeed. The picture changes below 10 kg/M, where D_T decreases and even becomes negative for effective monomers. The end group of a real polymer necessarily differs from the repeat unit; in order to exclude that the observed dependence on M_w was a simple

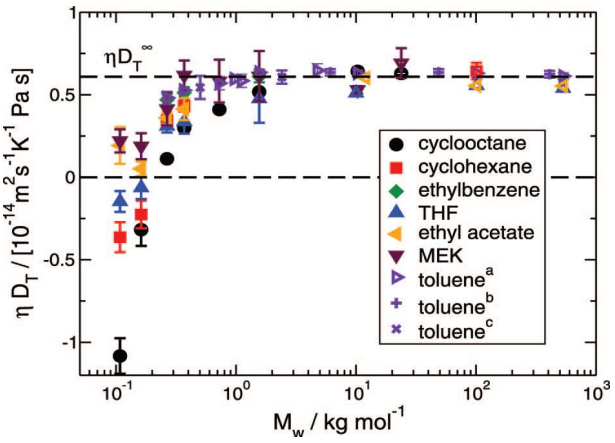

FIG. 24: Molecular-weight dependence of the reduced thermophoretic mobility ηD_T of polystyrene in various solvents at room temperature. For high polymers, the quantity ηD_T is independent of M_w and, more remarkably, independent of the solvent. Short polystyrene molecules, of less than 100 repeat units, diffuse more slowly, and are sensitive to details of the solvent molecules; in some cases, D_T even changes sign for effective monomers. Figure by courtesy of W. Köhler. (Reprinted with permission from Ref. [10]. Copyright 2008 American Chemical Society.)

end group effect, the authors of Ref. [10] studied two possible monomers, which correspond to the lowest values of M_w in Fig. 24: The first one, ethylbenzene (of molar mass 106) differs from a styrene unit merely by two hydrogen atoms; the second one, dimethylbutylbenzene (162 Dalton) may be viewed as a styrene with an aliphatic four-carbon group.

Fig. 24 shows the quantity ηD_T and thus reveals an additional feature with respect to the solvent properties. For long chains ηD_T takes almost identical values for all solvents, thus confirming that the difference in D_T stems to a large extent from the viscosity; cf. Table III. For short polystyrene chains, however, one observes a strong dispersion of the mobility from one solvent to another. For example, D_T in cyclohexane and cyclooctane differs by a factor of three, although the physico-chemical properties of these solvents are almost identical. This dispersion of the mobility indicates that for short chains, other solvent parameters besides the viscosity become relevant. The data of Fig. 24 are well fitted by the phenomenological law [9, 10]

$$D_T = D_T^\infty - \frac{\delta D_T}{N}, \tag{84}$$

where D_T^∞ is the mobility of high polymers and δD_T accounts for the variation for short chains.

A similar behavior has been observed by Chan et al. for polyethylene glycol (PEG) in aqueous solution [8]. Fig. 25 shows experimental data as a function of the chain length N, yet at constant constant concentration of ethylene units $c_{\rm eth} = 0.2$ M/l, which corresponds to a vol-

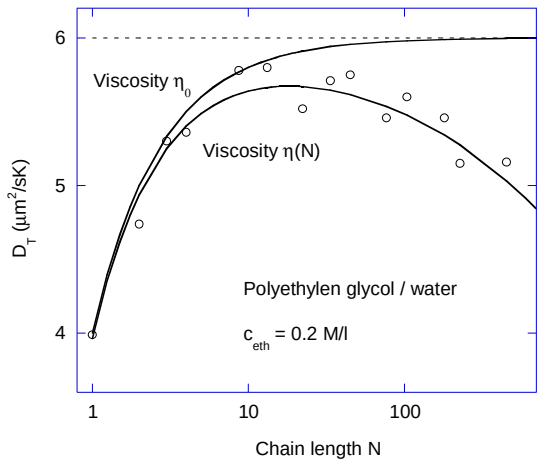

FIG. 25: Thermophoretic mobility D_T of polyethylen glycol as a function of the number of ethylen repeat units. The data are taken from Ref. [8]; the solid lines is given by $D_T^\infty - \delta D_T/N$, with $D_T^\infty = 6$ and $\delta D_T = 2$. The upper curve is calculated with constant viscosity η_0, the lower from the relation (74) with $\phi = 0.01$, $C = 0.9$, and $\nu = \frac{1}{2}$. The dashed line indicates D_T^∞.

ume fraction ϕ of about 1%. The initial increase of D_T is well fitted by Eq. (84), as shown by the curve calculated at constant viscosity η_0. The slow decrease at higher molecular weight is probably due to the increase of viscosity with the degree of polymerization, resulting in the modified mobility $(\eta_0/\eta)D_T$. The viscosity increases according to the Einstein relation (74), thus reducing the thermophoretic velocity. For the plot we use $\nu = \frac{1}{2}$ and the coefficient $C = 0.9$; the hydrodynamic volume is affected by hydration effects which are known to play an important role for PEG solutions [148].

These experiments suggest that the thermophoretic velocity consists of two contributions,

$$\mathbf{u} = \mathbf{u}_\infty + \delta\mathbf{u}, \tag{85}$$

where the first one stems from thermoosmotic flow around the solute, as outlined in Sect. IV, and the second one accounts for effects occurring for short chains. For the sake of simplicity, we do not distinguish between the bead radius a and the cut-off distance d_0 appearing in Eqs. (81) and (71) and thus have

$$\mathbf{u}_\infty = -\frac{\beta\varepsilon_0}{6\pi\eta a}\boldsymbol{\nabla}T. \tag{86}$$

The numerical prefactor is chosen such that the denominator corresponds to the Stokes friction coefficient $6\pi\eta a$.

Comparison with the mobility obtained from the single-bead model (81) shows that $\mathbf{u}_\infty$ corresponds to the term proportional to $\beta\varepsilon_1$, which derives from the van der Waals force exerted by the solvent on a solute bead. In view of (77) the flow driven by the molecular entropy remains to be evaluated; this directed Brownian motion results from thermodynamical forces [149]. Since motion driven by dispersion forces hardly depends on the chain length, the size-dependent term $\delta\mathbf{u}$ is related to thermal diffusion, that is, to the molecular entropy or to diffusive motion. The molecular-weight dependence of D_T and the significant increase with N are confirmed by molecular dynamics simulations of Zhang and Müller-Plathe [150]. A finite persistence length ℓ_p modifies the behavior of short chains.

VI. MICROFLUIDIC APPLICATIONS

Here we discuss a few examples of microfluidic applications, where thermal or chemical gradients are used for moving or accumulating molecular solutes and suspended particles or droplets in a controlled manner. Unlike electrophoresis, these fields operate equally well on charged and neutral systems. For thermophoresis of solid particles, the resulting velocity is independent of the size of the solute, whereas thermocapillary driving of liquid droplets and gas bubbles is proportional to their radius, and thus achieves much higher transport velocities.

A. Optothermal DNA trap in a microchannel

An optothermal trap for a DNA solution in a microchannel with an ambient flow of velocity v has been realized by Duhr and Braun [14]. As shown schematically in Fig. 26, a laser heats the grey region by a temperature ΔT; if the thermal conductivities of the fluid and outside material are comparable, the excess temperature profile $T - T_0 = \Delta T(r)$ is isotropic in 3-dimensional space and, at distances beyond the heated spot, decreases as $1/r$.

In an otherwise homogeneous solution, the temperature profile acts as an effective barrier that slows down the solute molecules approaching the heated zone, and that accelerates them once they have passed the temperature maximum. As a consequence, the solute accumulates in the upstream region where the thermal gradient is positive; its concentration decreases downstream of the thermal barrier. The total current of the molecular solute of concentration n,

$$\mathbf{J} = n\mathbf{v} - D\boldsymbol{\nabla}n - nD_T\boldsymbol{\nabla}T, \tag{87}$$

comprises a convection term $n\mathbf{v}$, diffusion with the Einstein coefficient D, and thermophoresis with the mobility $D_T > 0$. The steady state is reached if the overall current takes everywhere the constant value $\mathbf{J}_{\rm st} = n_0\mathbf{v}$.

The essential physics is grasped by a one-dimensioinal model, which neglects the velocity profile across the channel and accounts for the variation in the flow direction only. Since the thermal gradient modifies the mean molecular velocity, the constant steady-state current $\mathbf{J}_{\rm st}$ implies a non-uniform concentration [14],

$$n_{\rm st}(y) = n_0\frac{v}{D}e^{-\psi(y)}\int_y^\infty dy' e^{\psi(y')}, \tag{88}$$

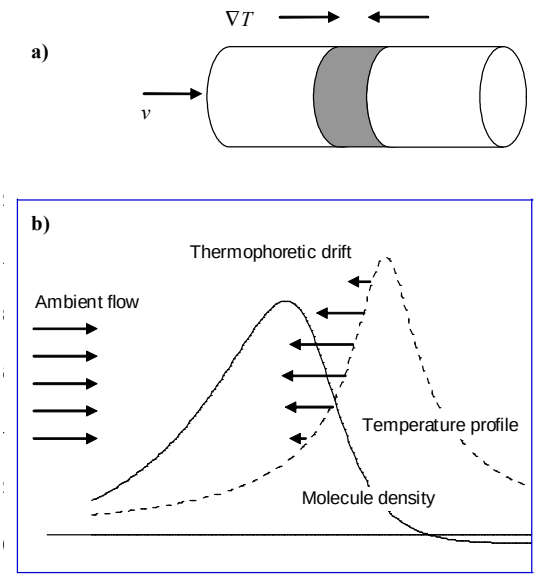

FIG. 26: a) Schematic view of a microchannel with ambient flow velocity v; local heating in the grey spot creates a temperature gradient along the channel. b) Temperature profile and steady-state solute concentration n in the microchannel; the horizontal line gives the mean concentration n_0. The arrows indicate the ambient flow v and the thermophoretic drift velocity $u = -D_T \nabla T$. After Ref. [14].

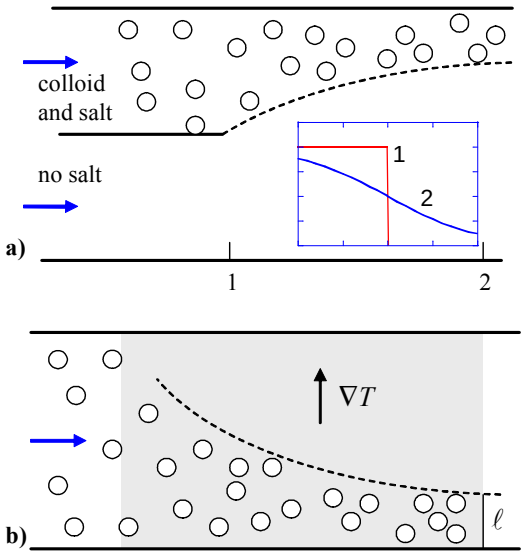

FIG. 27: a) Salinity-driven focussing of colloidal particles in a microchannel [151]; the inset shows the lateral variation of the salinity. At position 1, there is no salt present in the lower half channel. Downstream (to the right of position 1) the salt diffuses through the channel, resulting at position 2 in a lateral gradient of the order $\nabla n_0 \sim n_0/L$. This salinity gradient focusses the colloidal particles as indicated by the dashed line. Still further downstream, the salinity reaches a constant value across the channel, and the effect disappears. b) Thermal focussing in a microchannel with ambiant flow velocity v; a lateral temperature gradient is applied in the grey zone. Thermophoresis drives the colloidal particles to the colder side.

where y is the coordinate along the channel and the exponential factor is given by

$$\psi(y) = S_T \Delta T(y) - yv/D. \tag{89}$$

Far away from the heated spot, the concentration takes the constant value $n_{\rm st} = n_0$. The solid line of Fig. 26b displays the steady-state concentration $n_{\rm st}$ close to the heated spot: Accumulation upstream of the thermal barrier is followed by depletion below the mean value n_0 at the opposite side. With a maximum temperature increase of 16 K, Duhr and Braun obtained a 18 times higher DNA concentration.

According to Eq. (88) the enhancement factor varies exponentially with the dimensionless parameter $S_T \Delta T$; since the Soret coefficient increases with the molecular weight, longer chains accumulate more strongly. Moreover, the enhancement depends on the flow velocity v; its maximum occurs where v is comparable to the thermophoretic velocity u, that is, of the order of a few microns per second.

B. Lateral fields in a microchannel

Now we turn to the case where the external field is applied perpendicular to the flow. Consider a microchannel of width L, in which a colloidal suspension is injected as illustrated in Fig. 27a. For the sake of simplicity we neglect the velocity profile and assume a constant value v across the channel. Uncharged particles would, starting form the position 1, diffuse freely and explore the whole channel width after a time $\Delta t \sim L^2/D$, corresponding to a downstream distance $v\Delta t$.

On the contrary, focussing may occur for charged colloids in an electrolyte solution, as shown by Bocquet and co-workers [151, 152] in an experiment similar to Fig. 27a. The important point is that the Einstein coefficient D_s of salt ions much larger than D; their ratio is roughly given by that of the radii of the colloidal particles and the salt ions, $D_s/D \sim a/a_s \gg 1$. Thus after a time $\Delta t_s \sim L^2/D_s$, the salinity profile across the channel looks like curve 2 in the inset of Fig. 27a; because of $\Delta t_s \ll \Delta t$, particle diffusion is negligible. According to Eq. (31), the salinity gradient pushes the colloidal particles towards regions of higher electrolyte strength, and thus focusses the suspension as illustrated by the dashed line in the Figure. For a sufficiently negative value of the parameter γ, the particles would migrate in the opposite direction. Note that this effect vanishes further downstream, well beyond a distance $v\Delta t_s$, where the salinity reaches a constant value across the channel.

Similar effects occurs when applying a lateral temperature gradient, with the noticeable difference that its range along the channel is an experimental control parameter, contrary to the above salinity gradient. Moreover, heat conduction is much faster than ion diffusion; a thermal gradient can be switched on and off vary rapidly, whereas diffusion of salt ions over a 50 micron wide channel takes several seconds.

A possible experimental setup is shown in Fig. 27b, where a lateral temperature gradient $\nabla T = \Delta T/L$ is applied on a colloidal suspension in a channel with ambient flow velocity v. With a temperature difference $\Delta T \sim 25$ K over a width $L = 50\mu$m, and assuming a thermophoretic mobility $D_T \sim 10\ \mu\text{m}^2/\text{Ks}$, the particles migrate at a velocity $u = 5\mu$m/s and reach the steady state after the time L/u. The stationary lateral distribution reads as

$$n(x) = n_0 \frac{\ell}{L} \frac{e^{-x/\ell}}{1 - e^{-L/\ell}}, \tag{90}$$

where the vertical coordinate x is measured from the upper boundary ($0 \le x \le L$) and where n_0 is the initial uniform density. The characteristic length

$$\ell = \frac{D}{u_0}$$

plays the role of a sedimentation length. For the above parameters one finds $\ell = 2\mu$m; thus the particles are trapped in a micron size layer at the lower boundary. The steady-state distribution is readily obtained from the condition of zero current; there is no closed solution for the transient kinetics. The time dependent distribution function $n(x,t)$ has been given as series in powers of $e^{-L/\ell}$; a rather simple expression arises for the case of strong confinement $L \gg \ell$ [153].

C. Hydrodynamic attraction of confined colloids

We consider a thin film without ambient flow, where a temperature gradient drives the colloidal particles towards the lower boundary. Because of the hydrodynamic interactions with the boundary, the sedimentation kinetics of a particle close to a wall is an intricate problem. As the particle approaches the wall at a distance h, its velocity due to the buoyancy force decreases linearly with the ratio a/h [108, 154, 155]; on the other hand, the velocity u_0 driven by osmotic forces, such as electrophoresis or thermophoresis, is less sensitive to confinement and decreases as $(a/h)^3$ [156].

Here we are interested in the steady state, the vertical probability distribution of which is given in Eq. (90). Several experiments on micron-sized particles achieved a sedimentation length ℓ of the order of 1 μm, such that Brownian motion perpendicular to the confining plane is almost negligible. If the particle mass density exceeds that of the solvent by $\Delta\rho$, the buoyancy force even reduces the sedimentation length further,

$$\frac{1}{\ell} = \frac{u_0}{D} + \frac{\Delta\rho V_p g}{k_B T}. \tag{91}$$

For $\Delta\rho = 0.1$ g/cm^3 and a particle radius $a = 1\mu$m, one finds that ℓ is smaller than one micron. Then the colloidal particles are confined in vertical direction but still show two-dimensional diffusion along the plane. Electrostatic repulsion keeps the particle at a distance $h \approx a + \lambda$ from the wall, where λ is the Debye length.

The double-layer forces continue to pump fluid along the particle surface at a velocity given by Eq. (25), resulting in an outward vertical and an incoming radial flow. The radial component along the solid boundary acts as an attractive hydrodynamic force on neighbor particles [16, 17] and, at sufficiently high density, leads to the formation of hexagonal crystals. Such effects are well known form electrophoretic deposition; they are linear in an applied dc field, whereas high-frequency ac fields results in more complex dependencies [158–162].

First consider the simple case of an unconfined particle that is immobilized by an external force such as optical tweezers. The quasi-slip condition at the particle surface imposes a finite boundary velocity similar to Eq. (16),

$$\mathbf{n}\cdot\mathbf{u}|_P = 0, \quad \mathbf{t}\cdot\mathbf{u}|_P = u_0, \tag{92}$$

where $\mathbf{n}$ and $\mathbf{t}$ are radial and tangential unit vectors in polar coordinates r, θ. Imposing zero velocity at infinity, one finds

$$\mathbf{v}^{(0)} = u_0 \left[\mathcal{C}\mathbf{n}\left(\frac{a}{r} - \frac{a^3}{r^3}\right) - \frac{\mathcal{S}}{2}\mathbf{t}\left(\frac{a}{r} + \frac{a^3}{r^3}\right)\right], \tag{93}$$

with $\mathcal{C} = \cos\theta$ and $\mathcal{S} = \sin\theta$. In terms of hydrodynamic multipoles [163], this flow consists of a "stokeslet" proportional to $1/r$ and a "source doublet" proportional to $1/r^3$, which are driven by the external force and the quasi-slip at the surface, respectively. The velocity field is shown schematically in Fig. 28a.

Now we introduce a wall B at a distance h from the particle center. Stokes boundary conditions require both parallel and perpendicular velocity components to vanish at B; as is obvious from Fig. 28a, this is not satisfied by the velocity field $\mathbf{v}^{(0)}$. The method of reflections [108] provides an iterative scheme for improving the velocity field $\mathbf{u}$ such that it satisfies both the quasi-slip at the particle surface and the condition at the solid boundary, $\mathbf{u}|_B = 0$. In the first step we add a term $\hat{\mathbf{v}}^{(0)}$ that solves the force-free Stokes' equation $\boldsymbol{\nabla}^2\hat{\mathbf{v}}^{(0)} = 0$ and that cancels $\mathbf{v}^{(0)}$ at the wall, $(\mathbf{v}^{(0)} + \hat{\mathbf{v}}^{(0)})|_B = 0$. This additional flow may be viewed as arising from the mirror image of the particle with respect to the plane B. As shown in Fig. 28b, the image flow differs significantly from the original $\mathbf{v}^{(0)}$; in the language of hydrodynamic multipoles it comprises a "source doublet", in addition to the stokeslet and the source doublet present in $\mathbf{v}^{(0)}$.

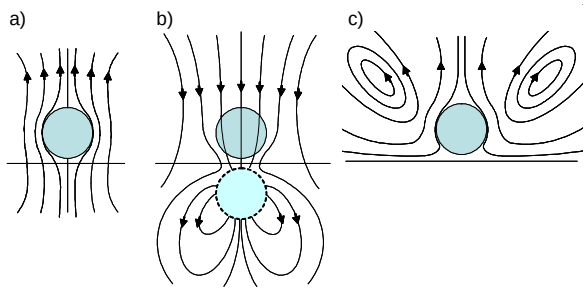

FIG. 28: Schematic view of the velocity fields close to a particle at a solid boundary. a) Flow pattern $\mathbf{v}^{(0)}$ due to the quasislip at the surface of an immobile particle in the absence of the wall. b) Velocity field $\hat{\mathbf{v}}^{(0)}$ due to an image particle. c) The superposition $\mathbf{u}^{(0)} = \mathbf{v}^{(0)} + \hat{\mathbf{v}}^{(0)}$ satisfies the stick boundary condition at the wall B. (Reprinted from Ref. [164].)

The superposition $\mathbf{u}^{(0)} = \mathbf{v}^{(0)} + \hat{\mathbf{v}}^{(0)}$ is illustrated in Fig. 28c; it satisfies the condition at B but not that at the particle surface P. An improved solution is obtained by projecting $\hat{\mathbf{v}}^{(0)}$ at the particle surface, that is, by adding a contribution $\mathbf{v}^{(0)}$ that is determined by $(\hat{\mathbf{v}}^{(0)} + \mathbf{v}^{(1)})|_P = 0$. The corresponding mirror flow $\hat{\mathbf{v}}^{(1)}$ is chosen such that it obeys $(\mathbf{v}^{(1)} + \hat{\mathbf{v}}^{(1)})|_B = 0$. By iterating this scheme one constructs a sequence $\mathbf{u}^{(k)}$, with $k = 0, 1, 2, ...$that converges towards the exact solution [164]. It turns out that the lowest order $k = 0$ is too small by a factor of about 2. The velocity at $k = 1$ provides a more satisfactory approximation, except at very short distances close to the particle. Higher orders $k \geq 2$ mainly modify the short-range behavior.

As shown schematically in Fig. 28c, the inward radial flow along the boundary acts as a hydrodynamic force $F(\rho) = 6\pi\eta a u_\rho$ on nearby particles; the resulting competition between diffusion and advection results in an enhancement of the steady-state probability distribution function $n(\rho) = n_0 e^{-V/k_B T}$, where the effective potential is defined through $F(\rho) = -\partial_\rho V$. For the experiments to be discussed below we truncate the series at linear order $k = 1$ [164],

$$\frac{V}{k_B T} = 8\frac{u_0 a}{D}\left(\frac{ah(a^2 q_3 - p_1 h^2)}{\hat{r}_h^3} - 6q_3\frac{a^3 h^3}{\hat{r}_h^5}\right). \qquad (94)$$

where the coefficients

$$p_1 = 1 + \frac{9}{8}\frac{a}{h}, \qquad q_3 = -1 - \frac{3}{8}\frac{a}{h},$$

depend on the ratio a/h; the quantity $\hat{r}_h = \sqrt{\rho^2 + 4h^2}$ is given by the horizontal spacing of the particles ρ and their vertical distance from the boundary h. The prefactor defines the dimensionless Péclet number

$$\mathrm{Pe}{=}u_0 a/D$$

which is the ratio of the advection velocity u_0 and that of diffusion over a particle size D/a. For large values, $\mathrm{Pe} \gg 1$, advection is faster than diffusion, and hydrodynamic interactions provide an efficient trap. The zero-order approximation $k = 0$ is obtained by putting $p_1 = 1$ and $q_3 = -1$; the resulting expression is identical to that given previously by Di Leonardo et al. [17].

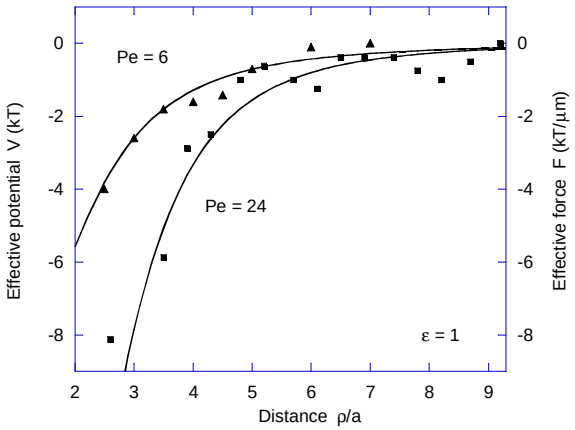

FIG. 29: Advection-driven attractive force of nearby particles as a function of their lateral distance. Experimental data of Weinert and Braun [16] for the effective potential V are indicated by triangles, those of Di Leonardo et al. [17] for the force $F = -\partial_\rho V$ by squares. The curves are calculated from (94) and $F = -\partial_\rho V$ with $\mathrm{Pe} = 6$ and 24, respectively.

Weinert and Braun investigated thermophoresis of polystyrene particles in a thin aqueous film; heating the upper boundary creates a vertical temperature gradient which pushes the particles towards the lower glass wall. The in-plane motion of the polystyrene beads is observed by single particle tracking: the statistical analysis of the two-dimensional pair correlation function gives the effective potential V in terms of the radial distance ρ [16]. Data points are given as triangles in Fig. 29. At the smallest investigated distance of two and a half particle radii, the attractive potential takes a value of about four times the thermal energy, which corresponds to an enhancement of the probability distribution $n(\rho)$ of almost two orders of magnitude. The theoretical curve has been calculated from Eq. (94) using $\mathrm{Pe} = 6$; the corresponding slip parameter $u_0 = 1.3$ μm/s roughly agrees with the numerical analysis of Ref. [16]. With the applied thermal gradient $\nabla T = 0.28$ K/μm, one calculates the transport coefficient $D_T \approx 5$ $\mu\mathrm{m}^2$/Ks, which lies in the range expected for weak electrolytes [42].

A direct measurement of the attractive force F has been reported by Di Leonardo and co-workers [17]. Using optical tweezers, these authors determined the radial attraction between silica beads ($a = 1\mu$m) in a water/alcohol mixture; their data are indicated in Fig. 29 by squares. The theoretical curve is calculated with the Péclet number $\mathrm{Pe} = 24$; thus the velocity scale $u_0 = -D_T \nabla T$ is four times larger than that of the ex-

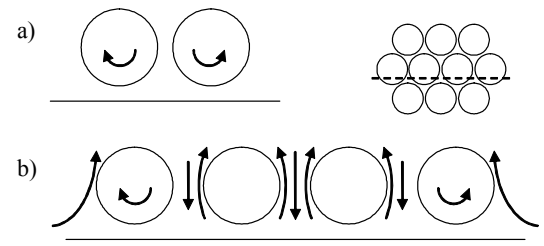

FIG. 30: a) The finite curl of the advection velocity field leads to a rotation of the neighbor particles. b) View of the velocity field across a small aggregate along the dashed line. In the middle of the aggregate, the lateral advection fields of the surrounding particles cancel. Only the outer particles rotate significantly; the slip flow of inner particles is compensated by the vertical fluid flow in the "chimneys". (Reprinted from Ref. [164].)

periment of Ref. [16].

The curl of the velocity field $\mathbf{u}$ exerts a torque on a neighbor bead; thus two nearby particles rotate in opposite direction as shown in Fig. 30a. Evaluating $\boldsymbol{\nabla} \times \mathbf{u}$ to leading order in ε and $1/\hat{r}_h$ one finds the frequency [164]

$$\Omega = 6u_0 h^2 a\rho/\hat{r}_h^5. \tag{95}$$

At sufficiently high particle density, the hydrodynamic forces favor the formation of cluster as illustrated in Fig. 30b; such two-dimensional crystals have indeed observed, both due to electroosmotic flow in an external field $\mathbf{E}$ [162] and its thermoosmotic counterpart in a temperature gradient $\boldsymbol{\nabla} T$ [16, 17]. Such clusters show an intricate flow pattern: The outer particles behave like those in a dimer; their rotational motion is maintained by the asymmetric radial flow, as shown in Fig. 30b. There is no flow towards the inner particles; the osmotic upward flow at the particle surface is counterbalanced by downward currents in the triangular space between adjacent particles. This rotational motion at a frequency of about 1 Hz of the outer particles has indeed been observed experimentally for polystyrene beads in an ac electric field [165]. A similar behavior with $\Omega \sim 1$ sec^{-1} is expected to occur for charged micron-size particles in a thermal gradient $\nabla T \sim 1$ K/μm.

D. Thermocapillary effects

So far we have discussed motion arising from thermoosmosis at solid-fluid interfaces. Microfluidic chemical reactors rely to a large extent on laser-induced manipulation of emulsion droplets and liquid films. Besides the electrostrictive or radiative pressure in normal direction, Marangoni forces parallel to the interface are commonly used in microfluidic devices [21–23]. As an efficient means of microactuation, local heating by laser absorption induces a temperature gradient which, in turn, modifies the energy density $\sigma(T)$ along the interface, and thus results in the gradient in the tangent plane,

$$\nabla_\parallel \sigma = \frac{3\kappa_s}{2\kappa_s + \kappa_d} \frac{d\sigma}{dT} \nabla_\parallel T, \tag{96}$$

where $\nabla_\parallel T$ denotes the parallel component of the applied gradient. The prefactor with the ratio of the droplet and solvent thermal conductivities is the same as in Eqs. (7) and (24). Thermocapillary forces have been used to control the spreading of micron-sized liquid films [166] and to move suspended gas bubbles [107, 167] or liquid droplets [168–171].

For a free droplet in a bulk liquid, the thermocapillary migration velocity is proportional to its radius a. The gradient $\nabla_\parallel \sigma$ exerts a lateral force on the fluid at both sides of the interface. In analogy to the case of hydrodynamic slip at a solid surface treated in Eq. (47), the macroscopic boundary conditions involve the changes of velocity Δv and shear stress $\Delta\Sigma$ through the interface. Anderson's solution for the droplet velocity in an unbounded outer fluid reads in our notation [70]

$$\mathbf{u} = -\frac{3\eta_d}{2\eta_s + 3\eta_d} \langle \Delta \mathbf{v} \rangle - \frac{a}{2\eta_s + 3\eta_d} \langle \Delta \boldsymbol{\Sigma} \rangle , \tag{97}$$

where η_d and η_s are the inside and outside viscosities, and $\langle ... \rangle$ denotes the orientational average along the particle surface. In the limit of a highly viscous droplet, $\eta_d \to \infty$, the second term vanishes and one recovers the velocity $\mathbf{u} = -\langle \Delta \mathbf{v} \rangle$ of a solid particle with no-slip conditions. For a micron-sized fluid droplet, on the other hand, the second term prevails because of the presence of the radius a, which is much larger than the range of the interface forces. The corresponding boundary condition requires that the thermocapillary term cancels the change of the shear stress through the interface, $\Delta\Sigma = \nabla_\parallel \sigma$. Assuming $\kappa_d = \kappa_s$ in (96) one finds

$$\mathbf{u} = -\frac{2}{3} \frac{a}{2\eta_s + 3\eta_d} \frac{d\sigma}{dT} \boldsymbol{\nabla} T. \tag{98}$$

The effective interface tension usually decreases with rising temperature, $d\sigma/dT < 0$. Then the droplet migrates along the applied gradient $\boldsymbol{\nabla} T$ towards higher temperatures. (Note that some authors define the derivative as its absolute value $|d\sigma/dT|$.)

By equilibrating the buoyancy of gas bubbles in a liquid with the thermocapillary force, Young et al. found the velocity to be proportional to the temperature gradient and to the radius [107]; these dependencies were confirmed for microemulsion droplets [168]. Studies on droplets moving on a solid surface revealed a more complex behavior [171–173], including contact angle hysteresis and a threshold value a_c for the radius; droplets smaller than a_c are pinned at the surface [173]. Brochard analyzed their shape and the underlying forces in terms of the spreading coefficient [172]. With typical gradients $-d\sigma/dT$ ∼a few mN m^{-1}K^{-1}, measured velocities for millimeter sized droplets are of the order of mm/s.

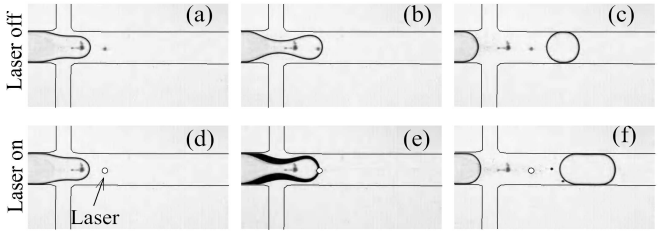

FIG. 31: Thermocapillary valve for water-in-oil droplets of variable size in a 200 micron tube. a) Water is injected from the left, and oil from the lateral channels. b) A neck forms and c) finally pinches off a droplet. The lower panel shows the same sequence, but with a laser heating the indicated spot. The resulting temperature gradient along the oil-water interface blocks formation of the neck and thus results in bigger drops. Figure by courtesy of J.-P. Delville. (Reprinted with permission from Ref. [174]. Copyright 2007 American Physical Society.)

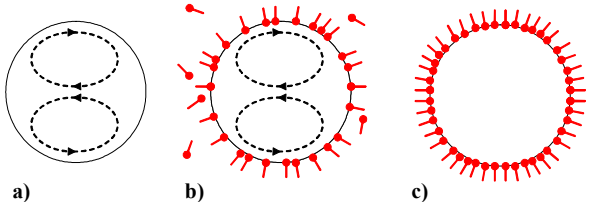

FIG. 32: Flow pattern inside a liquid droplet or gas bubble that moves to the left at a velocity u. a) The continuous tangential velocity at the fluid interface implies rolls inside the droplet. b) In the case of a weakly adsorbing surfactant, there is a constant rate of adsorption at the left side, then the molecules move with the interface along the droplet surface and desorb at the right side. c) A strongly adsorbing surfactant diffuses very little along the interface, and the droplet behaves like a solid particle.

Thermal actuation of droplets in nanofludic and microfluidic devices provides a useful tool for addressing chemical reactors [21–23]. Note that for a bubble size comparable to the pipe section, Eq. (98) ceases to be valid; the viscous stress occurs in the narrow range between the bubble and the channel border, leading to a migration velocity that is independent of the size [175].A thermocapillary valve in a cross-shaped microchannel has been realized by Baroud et al. [174]. The upper panel of Fig. 31 shows how the water finger advances in the oil phase, forms a neck, and finally pinches off a droplet. In the lower panel, absorption of laser light heats the tip of the finger, stabilizes the neck, and thus delays pinching. The blocking time increases linearly with the laser power, and so does the volume of the droplets. In order to single out the mechanism that inhibits neck formation, Baroud et al. tracked seeding particles inside the droplet and found convection rolls such that both fluids move along the interface towards the hot spot. This indicate an increase of tension with temperature, $d\sigma/dT > 0$, and has been related to the presence of surfactant molecules at the interface [176].

Adding surfactants reduces the thermocapillary velocity at the interface and thus slows down the droplet. At the phase boundary between two pure liquids, the tangential velocity is continuous across the interface whereas the normal component vanishes,

$$\mathbf{t}\cdot(\mathbf{v}_d-\mathbf{v}_b)=0, \qquad \mathbf{n}\cdot\mathbf{v}_d=0=\mathbf{n}\cdot\mathbf{v}_b. \tag{99a}$$

This means that the molecules at the interface have a finite velocity with respect to the center of the droplet, as illustrated in Fig. 32a; the velocity field of the bulk phase b in the laboratory frame is the same as that shown in Fig. 5. Weakly adsorbing surfactants diffuse between interfacial layer and bulk phases [177]. The surfactant current carried by the moving interface is maintained by a constant rate of adsorption on the left side in Fig. 32b, and desorption on the right side, resulting in an additional friction mechanism that enhances the effective droplet viscosity.

Strongly adsorbing surfactant molecules suppress the fluid character of the interface and change the hydrodynamic boundary conditions [178, 179]; Eq. (99a) is replaced by the stronger condition of zero velocity in the frame attached to the droplet,

$$\mathbf{v}_d=0=\mathbf{v}_b. \tag{99b}$$

As a consequence, the contribution proportional to $\langle\Delta\boldsymbol{\Sigma}\rangle$ in (97) disappears, and the droplet mobility is strongly reduced. Regarding the cross-over from the liquid to the solid interface, there is a close analogy to the suppression of hydrodynamic slippage in Eq. (47) as the slip length tends to zero. The resulting expression for the droplet velocity is identical to that of a solid particle and thus is independent of the radius. This has indeed been found in a recent experiment on nano-droplets in an AOT-water-oil emulsion [113].

Pieranski's observation of macroscopic reorganization of bicontinuous lyotropic crystals, provides a striking illustration for thermal effects in complex phases [20]. For example, 50-micron inclusions in the binary system water/$C_{12}EO_2$ changed their shape upon applying a weak temperature gradient $\nabla T = 1$ K/mm; for a given crystal orientation, positive and negative values of ∇T produce completely different effects. If some aspects are well understood in terms of de Gennes' work on the Soret motion in porous media [105], there remain open questions, in particular whether these experiments are described by thermoosmosis at rigid surfacted interfaces, or whether the capillary motion of the interface itself is an essential ingredient.

VII. CONCLUSION AND PERSPECTIVES

In the last years it has become clear that the thermal response of the electrolyte plays a major role for the transport of charged colloids [5, 42]. In many instances, this thermoelectric contribution to the mobility D_T exceeds the Ruckenstein term and thus dominates the colloidal Soret effect. The present understanding of thermophoresis relies on a single-particle picture, where D_T is independent of the colloidal volume fraction and, in the case of polyelectrolytes, of the chain length. Recent experiments show, however, that this picture ceases to be valid in semi-dilute systems where D_T depends on the volume fraction of a suspension of silica beads [96], and the molecular weight of NaPSS and DNA solutions [6, 33, 180]. At present is not clear to what extent hydrodynamic or electrostatic effects are responsible for these observations.

The temperature dependence of the mobility of charged colloids is strongly correlated with the thermal expansivity of water [33, 47] and shows a linear increase from 0° to 40° C. At present it is not clear whether this variation arises from the thermal response of the electrolyte, i.e., the thermoelectric coefficient (42), or whether the dispersion forces in (67) contribute to the temperature dependence. A particularly intriguing aspect occurs for dense peptide solutions: The positively charged poly-lysine shows a temperature dependent mobility similar to that of the negatively charged β-lactoglobulin, DNA, and NaPSS [33]; from the linear thermoelectric effect, however, one expects D_T to be proportional to the surface potential and thus an opposite temperature derivative for positive and negative valency.

As one of the most striking features of polymer thermophoresis in organic solvents, the mobility of high polymers is independent of the molecular weight [3], whereas a strong variation occurs for short chains of less than hundred repeat units. Recent work on polystyrene ranging from 1 to a few hundred repeat units, shed some light on this observation [10, 149]: In addition to the well-known constant mobility due to solute-solvent forces, there is a term proportional to the inverse gyration radius of the polymer. Still, this does not explain the negative D_T reported for 'light' polymers in 'heavy' solvents, such as PDMS (monomer mass $m = 74$ g/M) or polyethylene ($m = 28$ g/M) in cyclooctane ($m = 112$ g/M) [181].

Regarding molecular mixtures, experiments and numerical simulations give conclusive evidence that light and small solutes move to the warm, and large and heavy ones to the cold; yet this finding lacks a physical picture so far, and there is no satisfactory description for the volume and mass dependencies. We mention two experimental observations. Thermophoresis is sensitive to surface properties; grafting octadecyl groups on silica particles changes the sign of D_T and gives rise to an intricate temperature dependence [7]. On the other hand, deuteration of benzene or cyclohexane results in a significant isotope effect illustrated in Fig. 22; since the protonated and deuterated molecules are chemically identical, this indicates the Soret motion to be sensitive to the characteristic velocity $\sqrt{k_B T/m}$ of the molecular thermal agitation.

Acknowledgements

For helpful comments and stimulating discussions, the author is indebted to Y. Amarouchène, M.M. Bou-Ali, D. Braun, F. Cichos, J. Dhont, L. Foret, G. Galliéro, W. Köhler, K. Morozov, R. Piazza, P. Pieranski, and S. Wiegand. Thanks are due to S. Fayolle, A. Majee, J. Morthomas, T. Bickel, S. Le Boiteux, and Y. Leroyer for their collaboration, and to W. Köhler, J.-P. Delville, and M. Sano for the kind permission to reproduce original figures from their articles.

[1] S. de Groot and P. Mazur, *Non-equlibrium Thermodynamics* (North Holland Publishing, Amsterdam, 1962).
[2] E. Ruckenstein, J. Coll. Interf. Sci. **83**, 77 (1981).
[3] F. Brochard and P.-G. de Gennes, C. R. Acad. Sc. Paris Série II **293**, 1025 (1981).
[4] R. Piazza and A. Guarino, Phys. Rev. Lett. **88**, 2083021 (2002).
[5] S. A. Putnam and D. G. Cahill, Langmuir **21**, 5317 (2005).
[6] S. Duhr and D. Braun, PNAS **103**, 19678 (2006).
[7] H. Ning, J. Buitenhuis, J. Dhont, and S. Wiegand, J. Chem. Phys. **125**, 204911 (2006).
[8] J. Chan, J. Popov, S. Kolisnek-Kehl, and D. Leaist, J. Solution Chem. **32**, 197 (2003).
[9] J. Rauch and W. Köhler, Macromolecules **38**, 3571 (2005).
[10] D. Stadelmaier and W. Köhler, Macromolecules **41**, 6205 (2008).
[11] S. Wiegand, J. Phys. Cond. Matt. **16**, 357 (2004).
[12] R. Piazza and A. Parola, J. Phys. Cond. Matt. **15**, 153102 (2008).
[13] J. C. Giddings, Science **260**, 1456 (1993).
[14] S. Duhr and D. Braun, Phys. Rev. Lett. **97**, 038103 (2006).
[15] H.-R. Jiang, H. Wada, N. Yoshinaga, and M. Sano, Phys. Rev. Lett. **102**, 208301 (2009).
[16] F. Weinert and D. Braun, Phys. Rev. Lett. **27**, 425 (2008).
[17] D. Di Leonardo, F. Ianni, and G. Ruocco, Langmuir **25**, 4247 (2009).
[18] P. Baaske, F. Weinert, S. Duhr, K. Lemke, M. Russell, and D. Braun, PNAS **104**, 9346 (2007).
[19] I. Budin, R. Bruckner, and J. Szostak, J Am. Chem. Soc. **131**, 9628 (2009).
[20] P. Pieranski, Liquid Crystals **36**, 1049 (2010).
[21] T. Squires and S. Quake, Rev. Mod. Phys. **77**, 977 (2005).
[22] Z. Jiao, X. Huang, N.-T. Nguyen, and P. Abgrall, Microfluid. Nanofluid. **5**, 205 (2008).
[23] J.-P. Delville, M. Robert de Saint-Vincent, R. D.

Schroll, H. Chraïbi, B. Issenmann, R. Wunenburger, D. Lasseux, W. Zhang, and E. Brasselet, J. Opt. A: Pure Appl. Opt. **11**, 034015 (2009).
[24] C. Ludwig, Sitz. Ber. Akad. Wiss. Wien **20**, 539 (1859).
[25] C. Soret, Arch. Sci. Phys. Nat. **2**, 48 (1879).
[26] L. Longsworth, J. Phys. Chem. **61**, 1557 (1957).
[27] P. Snowdon and J. Turner, Trans. Faraday Soc. **56**, 1409 (1960).
[28] D. R. Caldwell, J. Phys. Chem. **77**, 2004 (1973).
[29] D. R. Caldwell and S. A. Eide, Deep Sea Research Part A, Oceanographic Research Papers **28**, 1605 (1981).
[30] F. S. Gaeta, G. Perna, G. Scala, and F. Bellucci, J. Phys. Chem. **86**, 2967 (1982).
[31] H. Yow and J. Lin, J. Solution Chem. **12**, 487 (1983).
[32] S. Iacopini and R. Piazza, Europhys. Lett. **63**, 247 (2003).
[33] S. Iacopini, R. Rusconi, and R. Piazza, Eur. Phys. J. E **19**, 59 (2006).
[34] K. Nachtigall and G. Meyerhoff, Makromol. Chemie **33**, 85 (1959).
[35] J. Giddings, K. Caldwell, and M. N. Myers, Macromolecules **9**, 106 (1976).
[36] M. Giglio and A. Vendramini, Phys. Rev. Lett. **38**, 26 (1977).
[37] M. Schimpf and J. Giddings, Macromolecules **20**, 1561 (1987).
[38] C. Debuschewitz and W. Köhler, Phys. Rev. Lett. **87**, 055901 (2001).
[39] B. Derjaguin and G. Sidorenkov, Dokl. Acad. Nauk SSSR **32**, 622 (1941).
[40] B. Derjaguin, N. Churaev, and V. Muller, *Surface forces* (Plenum, New York, 1987).
[41] K. I. Morozov, JETP **88**, 944 (1999).
[42] A. Würger, Phys. Rev. Lett. **101**, 108302 (2008).
[43] S. N. Rasuli and R. Golestanian, Phys. Rev. Lett. **101**, 108301 (2008).
[44] G. Guthrie Jr., J. N. Wilson, and V. Schomaker, J. Chem. Phys. **17**, 310 (1949).
[45] P. Staffeld and J. Quinn, J. Coll. Interf. Sci **130**, 88 (1989).
[46] J. L. Anderson and D. C. Prieve, Sep. Purif. Meth. **13**, 67 (1984).
[47] H. Brenner, Phys. Rev. E **74**, 036306 (2006).
[48] R. D. Astumian, PNAS **104**, 3 (2007).
[49] J. Tyndall, Proc. R. Inst. G.B. **6**, 1 (1870).
[50] W. Crookes, Proc. Roy. Soc. A **23**, 373 (1875).
[51] O. Reynolds, Phil. Trans. Roy. Soc. **170**, 727 (1879).
[52] J. Maxwell, Phil. Trans. R. Soc. **170**, 231 (1879).
[53] P. Epstein, Z. Phys. **54**, 537 (1929).
[54] L. Waldmann, Z. Naturforsch. **14a**, 589 (1959).
[55] F. Zheng, Adv. Coll. Interf. Sci. **97**, 255 (2002).
[56] D. Enskog, Physik. Zeits. **12**, 56 (1911).
[57] D. Enskog, Physik. Zeits. **12**, 533 (1911).
[58] S. Chapman, Philos. Trans. **A217**, 184 (1917).
[59] S. Chapman and T. Cowling, *The Mathematical Theory of Non-uniform Gases, 3rd ed.* (Cambridge University Press, 1970).
[60] W. Furry, R. Clark Jones, and L. Onsager, Phys. Rev. **55**, 1083 (1939).
[61] W. Watson and D. Woernley, Phys. Rev. **63**, 181 (1943).
[62] L. Waldmann, Z. Naturforsch. **4a**, 105 (1949).
[63] E. Lieb, Physica A **263**, 491 (1999).
[64] C. Gruber and J. Piasecki, Physica A **268**, 412 (1999).
[65] P. Meurs, C. van de Broeck, and A. Garcia, Phys. Rev. E **70**, 051109 (2004).
[66] D. Grier, Nature **424**, 810 (2003).
[67] M. Braibanti, D. Vigolo, and R. Piazza, Phys. Rev. Lett. **100**, 108303 (2008).
[68] D. Braun and A. Libchaber, Phys. Rev. Lett. **89**, 188103 (2002).
[69] F. Weinert and D. Braun, Nano Letters **9**, 4264 (2009).
[70] J. L. Anderson, Annu. Rev. Fluid Mech. **21**, 61 (1989).
[71] P. C. Hiemenz and R. Rajagopalan, *Principles of Colloid and Surface Chemistry* (Dekker, 1997).
[72] A. Würger, Phys. Rev. Lett. **98**, 138301 (2007).
[73] J. Stratton, *Electromagnetic theory* (Mc Graw-Hill, New York, 1941).
[74] L. Landau and E. Lifshitz, *Electrodynamics of Continuous Media* (Pergamon Press, Oxford, 1960).
[75] S. Fayolle, T. Bickel, and A. Würger, Phys. Rev. E **77**, 041404 (2008).
[76] J. C. Giddings, P. M. Shinudu, and S. N. Semenov, J. Coll. Interf. Sci. **176**, 454 (1995).
[77] W. Russel, D. Saville, and W. Schowalter, *Colloidal Dispersions* (Cambridge University Press, 1989).
[78] A. Ramos, H. Morgan, N. Green, and A. Castellanos, J. Phys. D: Appl. Phys. **31**, 2338 (1998).
[79] K.-R. Huang, J.-S. Chang, S. Chao, K.-C. Wu, C.-K. Yang, C.-Y. Lai, , and S.-H. Chen, J. Appl. Phys. **104**, 064702 (2008).
[80] J. L. Anderson and D. C. Prieve, Langmuir **7**, 403 (1991).
[81] S. Dukhin and B. Derjaguin, *Electrokinetic Phenomena, Surface and Colloid Science Vol. 7* (Wiley, New York, 1974).
[82] R. O'Brien, J. Interf. Coll. Sci. **92**, 204 (1983).
[83] D. Prieve, J. Anderson, J. Ebel, and M. Lowell, J. Fluid Mech. **148**, 247 (1984).
[84] D. Prieve and R. Roman, J. Chem. Soc. Faraday Trans. **83**, 1287 (1987).
[85] J. Lyklema, *Fundamentals of Interface and Colloid Science, Vol. II: Solid-liquid interfaces* (Academic Press, 1995).
[86] A. Moreira and R. Netz, Phys. Rev. Lett. **87**, 078301 (2001).
[87] C. Fleck and R. Netz, Phys. Rev. Lett. **95**, 128101 (2005).
[88] L. Foret, R. Kühn, and A. Würger, Phys. Rev. Lett. **89**, 156102 (2002).
[89] J. N. Agar, C. Y. Mou, and J. Lin, J. Phys. Chem. **93**, 2079 (1989).
[90] V. N. Sokolov, L. P. Safonova, and A. A. Pribochenko, J. Solution Chem. **35**, 1621 (2006).
[91] E. D. Eastman, J. Am. Chem. Soc. **50**, 283 (1928).
[92] D. Vigolo, S. Buzzaccaro, and R. Piazza, Langmuir **26**, 7792 (2010).
[93] S. Fayolle, T. Bickel, S. Le Boiteux, and A. Würger, Phys. Rev. Lett. **95**, 208301 (2005).
[94] H. Ning, J. K. G. Dhont, and S. Wiegand, Langmuir **24**, 2426 (2008).
[95] R. Rusconi, L. Isa, and R. Piazza, J. Opt. Soc. Am. B **21**, 605 (2004).
[96] N. Ghofraniha, G. Ruocco, and C. Conti, Langmuir **25**, 12495 (2009).
[97] J. Dhont, J. Chem. Phys. **120**, 1632 and 1642 (2004).
[98] A. Würger, Langmuir **25**, 6696 (2009).
[99] D. R. Lide, *CRC Handbook of Chemistry and Physics* (CRC Press, 2005).

[100] R. Piazza, S. Iacopini, and B. Triulzi, Phys. Chem. Chem. Phys. **6**, 1616 (2004).

[101] G. Rainaldi, A. Calcabrini, and M. Santini, J. Mat. Sci.: Materials and Medicine **9**, 755 (1998).

[102] C. Neto, D. Evans, E. Bonaccurso, H.-J. Butt, and V. Craig, Rep. Prog. Phys. **68**, 2859 (2005).

[103] E. Lauga, M. Brenner, and H. Stone, in *Handbook of Experimental Fluid Dynamics*, edited by C. Tropea, A. L. Yarin, and J. Foss (Springer, Berlin Heidelberg New York, 2007).

[104] L. Joly, C. Ybert, E. Trizac, and L. Bocquet, J. Chem. Phys. **125**, 204716 (2006).

[105] P.-G. de Gennes, C. R. Acad. Sc. Paris Série II **295**, 959 (1982).

[106] J. Morthomas and A. Würger, J. Phys. Cond. Matt. **21**, 035103 (2009).

[107] N. Young, J. Goldstein, and M. Block, J. Fluid Mech. **6**, 350 (1959).

[108] J. Happel and H. Brenner, *Low Reynolds Number Hydrodynamics* (Prentice Hall, New Jersey, 1965).

[109] A. Ajdari and L. Bocquet, Phys. Rev. Lett. **96**, 186102 (2006).

[110] A. Khair and T. Squires, Phys. Fluids **21**, 042001 (2009).

[111] D. Henry, Proc. Royal Soc. London **133**, 106 (1931).

[112] F. Morrison, J. Coll. Interf. Sci. **34**, 210 (1970).

[113] D. Vigolo, G. Brambilla, and R. Piazza, Phys. Rev. E **75**, 040401 (2007).

[114] S. A. Putnam, D. G. Cahill, and G. C. L. Wong, Langmuir **23**, 9221 (2007).

[115] J. Morthomas and A. Würger, Eur. Phys. J. E **101**, 168301 (2008).

[116] E. Bringuier and A. Bourdon, Phys. Review E **67**, 114041 (2003).

[117] J. K. G. Dhont, S. Wiegand, S. Duhr, and D. Braun, Langmuir **23**, 1674 (2007).

[118] J. Dhont and W. Briels, Eur. Phys. J. E **25**, 61 (2008).

[119] H. Lekkerkerker, W. C.-K. Poon, P. N. Pusey, A. Stroobants, and P. Warren, Europhys. Lett. **20**, 529 (1992).

[120] L. Garrido, ed., *Complex fluids*, vol. 415 of *Lecture Notes in Physics* (Springer, Berlin, 1993).

[121] B. Derjaguin, G. Sidorenkov, E. Zubashchenkov, and E. Kiseleva, Kolloidn. Zh. **9**, 335 (1947).

[122] S. N. Semenov and M. E. Schimpf, Phys. Rev. E **69**, 011201 (2004).

[123] M. Han, J. Colloid Interf. Sci. **284**, 339 (2005).

[124] G. McNab and A. Meisen, J. Colloid Interf. Sci **44**, 339 (1973).

[125] P.-G. de Gennes, *Scaling Concepts in Polymer Physics* (Cornell University Press, Ithaca, 1979).

[126] I. Teraoka, *Polymer Solutions: An Introduction to Physical Properties* (Wiley, 2002).

[127] K. Zhang, M. Briggs, R. Gammon, J. Sengers, and J. Douglas, J. Chem. Phys. **111**, 2270 (1999).

[128] M. E. Schimpf, in *Thermal Nonequilibrium Phenomena in Fluid Mixtures*, edited by W. Köhler and S. Wiegand (Springer, Berlin Heidelberg New York, 2002).

[129] J. Rauch and W. Köhler, Phys. Rev. Lett. **88**, 185901 (2002).

[130] M. Hartung, J. Rauch, and W. Köhler, J. Chem. Phys. **125**, 214904 (2006).

[131] M. Schimpf and S. Semenov, J. Phys. Chem. B **104**, 9935 (2000).

[132] P. Rossmanith and W. Köhler, Macromolecules **29**, 3203 (1996).

[133] W. Enge and W. Köhler, Eur. Phys. J. E **15**, 265 (2004).

[134] J. Koetz and S. Kosmella, *Polyelectrolytes and Nanoparticles* (Springer, Berlin, 2007).

[135] A. Perronace, C. Leppla, F. Leroy, B. Rousseau, and S. Wiegand, J. Chem. Phys. **116**, 3718 (2002).

[136] R. Kita, P. Polyakov, and S. Wiegand, Macromolecules **40**, 1638 (2004).

[137] P. Polyakov, J. Luettmer-Strathmann, and S. Wiegand, J. Phys. Chem. B **110**, 26215 (2006).

[138] G. Wittko and W. Köhler, Europhys. Lett. **78**, 46007 (2007).

[139] B. Hafskjold, T. Ikeshoji, and S. K. Ratkje, Mol. Phys. **80**, 1389 (1985).

[140] D. Reith and F. Müller-Plathe, J. Chem. Phys. **112**, 2436 (2000).

[141] P. Blanco, M. Bou-Ali, J. Platten, P. Urteaga, J. Madariaga, and C. Santamaria, J. Chem. Phys. **129**, 174504 (2008).

[142] K. Denbigh, Trans. Faraday Soc. Trans. Faraday Soc **48**, 1 (1952).

[143] E. Dougherty and H. Drickamer, J. Phys. Chem. **59**, 443 (1955).

[144] K. Shukla and A. Firoozabadi, Ind. Chem. Eng. Res. **37**, 3331 (1998).

[145] L. J. T. M. Kempers, J. Chem. Phys. **115**, 6330 (2001).

[146] P.-A. Artola and B. Rousseau, Phys. Rev. Lett. **98**, 125901 (2007).

[147] G. Galliero and S. Volz, J. Chem. Phys **128**, 064505 (2008).

[148] C. Branca, S. Magazc, G. Maisano, F. Migliardo, P. Migliardo, and G. Romeo, J. Phys. Chem. B **106**, 10272 (2002).

[149] A. Würger, Phys. Rev. Lett. **102**, 078302 (2009).

[150] M. Zhang and F. Müller-Plathe, J. Chem. Phys. **125** (2006).

[151] B. Abécassis, C. Cottin-Bizonne, C. Ybert, A. Ajdari, and L. Bocquet, Nature Materials **7**, 785 (2008).

[152] J. Palacci, B. Abécassis, C. Cottin-Bizonne, C. Ybert, and L. Bocquet, Phys. Rev. Lett. **104**, 138302 (2010).

[153] Y. Leroyer and A. Würger, J. Phys. Cond. Matt. **22**, 195104 (2010).

[154] H. Brenner, Chem. Eng. Sci. **16**, 242 (1961).

[155] T. Squires, J. Fluid Mech. **443**, 403 (2001).

[156] H. Keh and J. Anderson, J. Fluid Mech. **153**, 417 (1985).

[157] T. Squires and M. Brenner, Phys. Rev. Lett. **85**, 4976 (2000).

[158] M. Giersig and P. Mulvaney, Langmuir **9**, 3408 (1993).

[159] M. Böhmer, Langmuir **12**, 1996 (1996).

[160] M. Trau, D. Saville, and I. Aksay, Nature **13**, 6375 (1997).

[161] S.-R. Yeh, M. Seul, and B. Shraiman, Nature **386**, 57 (1997).

[162] W. Ristenpart, I. Aksay, and D. Saville, Phys. Rev. E **69**, 021405 (2004).

[163] J. Blake, Proc. Camb. Phil. Soc. **70**, 303 (1971).

[164] J. Morthomas and A. Würger, Physical Review E **81**, 051405 (2010).

[165] J. Santana-Solano, D. Wu, and D. Marr, Langmuir **22**, 2006 (2006).

[166] N. Garnier, R. Grigoriev, and M. Schatz, Phys. Rev. Lett. **91**, 054501 (2003).

[167] A. Ohta, A. Jamshidi, J. Valley, H.-Y. Hsu, and M. Wu, Appl. Phys. Lett. **91**, 074103 (2007).
[168] K. Barton and R. Subramanian, J. Colloid Interf. Sci **133**, 211 (1989).
[169] K. Kotz, K. Noble, and G. Faris, Appl. Phys. Lett. **85**, 2658 (2004).
[170] S. Rybalko, N. Magome, and K. Yoshikawa, Phys. Rev. E **70**, 046301 (2004).
[171] V. Pratap, N. Moumen, and R. Subramanian, Langmuir **24**, 5185 (2008).
[172] F. Brochard, Langmuir **5**, 437 (1989).
[173] J. Chen, S. Troian, A. Darhuber, and S. Wagner, J. Appl. Phys. **97**, 014906 (2005).
[174] C. Baroud, J.-P. Delville, F. Gallaire, and R. Wunenburger, Phys. Rev. E **75**, 046302 (2007).
[175] E. Lajeunesse and G. Homsy, Phys. Fluids **15**, 308 (2003).
[176] E. Verneuil, M. Cordero, F. Gallaire, and C. Baroud, Langmuir **25**, 5127 (2009).
[177] Z. Khattari, P. Steffen, and T. Fischer, J. Phys. Cond. Matt. **14**, 4823 (2002).
[178] H. S. Kim and R. Subramanian, J. Colloid Interf. Sci **127**, 417 (1989).
[179] H. S. Kim and R. Subramanian, J. Colloid Interf. Sci **130**, 112 (1989).
[180] P. Reineck, C. Wienken, and D. Braun, Electrophoresis **31**, 279 (2010).
[181] D. Stadelmaier and W. Köhler, Macromolecules **42**, 9147 (2009).